The Effects of Contact Metamorphism by Diabase Intrusion on the Carbon and Sulfur Bearing Phases in the Siltstones of the Culpeper Basin

Emma Teresa Teeter Tulsky

Thesis submitted to the faculty of the Virginia Polytechnic Institute and State University in partial fulfillment of the requirements for the degree of

Master of Science

In

Geosciences

Benjamin C. Gill, Co-Chair

Mark J. Caddick, Co-Chair

Kenneth A. Eriksson

Robert J. Tracy

May 3, 2016

Blacksburg, VA

Keywords: Contact metamorphism, Geochemistry, Intrusions, Sulfur, Carbon, Iron, Volatile flux

The Effects of Contact Metamorphism by Diabase Intrusion on the Carbon and Sulfur Bearing Phases in the Siltstones of the Culpeper Basin

Emma Teresa Teeter Tulsky

ABSTRACT

Many of the large igneous provinces during the Phanerozoic have been temporally linked to mass extinction events. The intrusion of magma into country rock has been hypothesized to facilitate the release of carbon and sulfur bearing volatiles and has been proposed as one of mechanisms that drove these mass extinctions. In this study I examine a dike of the Central Atlantic Magmatic Province and its interaction with adjacent sedimentary rocks in the Culpeper Basin of Virginia. Sampling was done at the 0.5 m scale along transects of sedimentary lithologies perpendicular to the ~170 m wide diabase intrusion. The observed mineralogical and geochemical changes in sedimentary rocks occur in a much narrower zone from the intrusion than predicted by the applied thermal model. Carbon isotopes of organic matter within the sedimentary rocks are enriched in ^{13}C toward the intrusion indicating the generation of thermogenic methane within the first meter from the intrusion. Additionally, geochemical and petrologic textures suggest the addition of magmatic sulfur into the country rock, shown through the isotopic signatures of sulfide minerals with mantle compositions. The possible thermal break down of sedimentary pyrite is evidenced by highly negative isotopic composition of sulfide minerals and general lack of pyrite. I suggest that sedimentary pyrite initially reacted to pyrrhotite, which was then converted to chalcopyrite through reactions with copper in fluids derived from the magma. These reactions also allowed for the formation of magnetite, which is elevated near the dike-sedimentary contact and at the end of the transect. A simple illustrative model of a hypothesis of fluid flow along the bed is used to explain

the observed isotopic signatures and mineralogical changes along the transect. This study highlights how models for volatile generation through magma-country rock interaction may have overestimated the volatile fluxes from these environments and the roles that heterogeneity of sedimentary rocks and kinetic factors may have in the variance in these fluxes.

The Effects of Contact Metamorphism by Diabase Intrusion on the Carbon and Sulfur Bearing Phases in the Siltstones of the Culpeper Basin

Emma Teresa Teeter Tulsky

General Audience Abstract

The intrusion of large bodies of magma called large igneous provinces have been temporally linked to mass extinction events throughout geologic time. This intrusion of magma into country rock has been hypothesized to facilitate the release of carbon and sulfur bearing gases and has been proposed as one of mechanisms that drove these mass extinctions. In this study I examine a dike of the Central Atlantic Magmatic Province and its interaction with adjacent sedimentary rocks in the Culpeper Basin of Virginia. Sampling was done along beds of sedimentary lithologies perpendicular to the ~170 m wide igneous intrusion. Geochemical and mineral analyses found that changes in mineralogy and geochemistry were in a narrower zone than predicted by the applied thermal model. Carbon isotopes of organic matter within the sedimentary rocks are enriched in ^{13}C toward the intrusion indicating thermogenic methane generation within the first meter from the intrusion. Additionally, geochemical and mineral textures suggest the addition of magmatic sulfur into the country rock which was shown through the isotopic signatures of sulfide minerals with mantle compositions. A simple illustrative model of a hypothesis of fluid flow along the bed is used to explain the observed isotopic signatures and mineralogical changes along the transect. This study highlights how models for volatile generation through magma-country rock interaction may have overestimated the volatile fluxes from these environments and the roles that heterogeneity of sedimentary rocks and kinetic factors may have in the variance in these fluxes.

Dedication

I would like to dedicate this thesis to Dr. Benjamin Gill.
Thank you for taking me on as an undergraduate and seeing potential in me that I didn't. You have shown me what it truly means to be passionate about geology and inspired me to pursue this graduate degree. I couldn't have done it without your guidance and support and I am so grateful to have had you as an advisor and a friend.

Acknowledgements:

First and foremost I want to thank my advisors Benjamin Gill and Mark Caddick for creating this project and guiding me along the way. Thank you for providing me with insight and constructive criticism throughout these last two/three years.

I would also like to thank my other committee members Kenneth Eriksson and Robert Tracy for their insightful comments and general interest in the topic. Thank you for going out of your way to help me when I needed it.

I would like to thank the Luck Stone Co. for allowing me to access their Fairfax Quarry and collect my samples.

A huge thank you to the Petrology lab group. You guys have always been there for me when I needed it most. Calvin- Thank you for making the time to help me when I didn't understand Python or Perplex you are truly a life saver. Allie- Thank you for always being upbeat and positive when I was down. Jen- Thank you for having confidence in me and telling me I was going to be fine. Kirk- It has been so much fun being officemates with you.

Thank you to the Seddies for your support along the way. Matt- you are a fantastic scientist and a great friend, thank you for all the support and help these last three years. Teddy- I wouldn't have made it this far without your guidance.

A giant thank you to my best friend Sarah, who has been there for me since freshman year. You have been my go to through everything and I am so happy to call you my best friend.

I also want to thank my family for their love and support these last two years. You all have been so proud of me and encouraged me to be my best. Thank you for always being there when I needed to just talk. Mom- You have always been my number one support in whatever it is that I do and I am so happy to have such a supportive mother. Dad- Thank you for listening when I was struggling in school and providing guidance when I felt lost.

Lastly I want to thank Tucker. I could not have done this without him; he provided me with the slove and affection I needed on the saddest of days. His bright smile and goofiness has brought happiness to my life these last two years. Here's to many more adventures together!

Table of Contents

1. Introduction

i. Overview of study

Numerous Phanerozoic extinction events are temporally associated with the emplacement of large igneous provinces (LIPs) (Stothers 1993; Courtillot and Renne 2003; Wignall 2001). While the exact mechanisms of extinction are debated, most models link the extinctions to LIP emplacement through the release of volatiles from the eruptions (Wignall 2001). For example it is suggested that large quantities of greenhouse gases are emitted from LIPs, driving dramatic changes in climate (Wignall 2005; Pálfy et al. 2000; McElwain, Beerling, and Woodward 1999). It has also been proposed that the volcanism associated with LIPs could also trigger feedbacks in the Earth climate system. For example, LIP-induced climatic warming could drive the destabilization of methane clathrates in ocean sediments, driving additional greenhouse gas and further climatic warming (Wignall 2005). The source of gases released by LIPs has been linked to the volcanic provinces themselves as well as the devolatilization of carbon within the country rock surrounding them (Aarnes et al. 2010; Agirrezabala et al. 2014; Aarnes, Svensen, et al. 2011). Additionally, the decomposition of pyrite through thermal alteration can lead to the release of SO_2 gas into the atmosphere, temporarily causing a cooling effect on time scales of 10^3–10^4 years (Yallup, Edmonds, and Turchyn 2013). Given the potential for host sedimentary rocks to contribute significantly to the volatile budget of LIP eruptions, there is a need for additional, careful field-based studies that quantify the relative contributions of these potential sources of gas.

Previous studies have looked at the possible effects of heating organic carbon in sedimentary rocks by contact metamorphism and the potential release of carbon bearing volatiles. A study of a sill intrusion into organic-rich sediments in the Isle of Skye, Scotland

found a decrease in total organic carbon content and an enrichment in $\delta^{13}C$ of organic carbon proximal to the sill, and related those signatures to a release of thermogenic methane (Yallup, Edmonds, and Turchyn 2013). Additional studies of organic-rich sedimentary rocks such as coal and mudstones that have been intruded by igneous bodies have also shown that there is a possible breakdown of organic matter and the generation of large amounts of hydrocarbons and other carbon-bearing volatiles, predominantly in the form of isotopically light thermogenic methane which is then released to the atmosphere (Aarnes, Svensen, et al. 2011; Agirrezabala et al. 2014; Cooper et al. 2007). Alternatively, case studies by Yoksoulian et al. (2016) and Gröcke et al. (2009) have shown that despite evidence for the maturation of organic matter in the sedimentary rocks towards the igneous body, there is little to no evidence for significant loss of carbon from the sedimentary rock. Thus, constraining of the potential release of carbon-bearing volatiles, particularly methane, in these intrusive environments is still debated, motivating this study.

Few studies have been conducted to examine and quantify the potential for the release of sulfur-bearing volatiles through the intrusion of dikes and sills into sedimentary rocks. Yallup et al. (2013) found that the sulfide content decreases within the sedimentary rocks proximal to a mafic sill. This lead them to conclude that sulfur is released from the sedimentary rocks during contact metamorphism through the thermal breakdown and oxidation of pyrite to pyrrhotite during sill emplacement, which agrees with the experimental studies of Yamamoto (1984), Hu et al. (2006) and Toulmin & Barton (1964). This decomposition of pyrite and loss of sulfur from the country rock is also seen in many platinum-group-element ore deposits where pyrite forms pyrrhotite and free sulfur that can form either SO_2 or H_2S in the fluid; the isotopic composition of some dikes supports the release of sulfur bearing volatiles from

sedimentary rocks and into the magma (Andrews and Ripley 1989; Ripley and Li 2003). Furthermore, a study of the thermal effects on sulfur isotopic composition of organic matter shows the enrichment of ^{34}S upon heating with the generation of H_2S gas, implying a loss of sulfide upon heating (Amrani, Lewan, and Aizenshtat 2005). However more research needs to be conducted on how sulfide minerals within sediments behave in these systems to gain a better understanding of the processes taking place. Based on this previous research I hypothesize that chemical and isotopic signatures indicative of the release of sulfur species should be preserved in the sedimentary rocks proximal to dike intrusions. I test this hypothesis here by coupling sulfur and carbon analyses of a suite of rocks with numerical techniques to give insight into the fluid and mineralogical processes that occur within the sedimentary country rock during contact heating.

This field-based study focuses on processes associated with the emplacement of an individual dike of the Central Atlantic Magmatic Province (CAMP) into the siltstones and shales of the Newark Supergroup in the Culpeper Basin of Centreville, Virginia. CAMP magmatism was contemporaneous with the Triassic-Jurassic (T-J) mass extinction (Marzoli et al. 2004; Courtillot and Renne 2003) and has been proposed as the main driver of the extinction (McElwain, Beerling, and Woodward 1999; Marzoli et al. 2004; Hesselbo et al. 2002). This extinction event, one of the Phanerozoic "big five", is associated with the loss of ~ 40% of genera (Sepkoski 1996), including the loss of ~ 30% of marine genera and ~ 50% of tetrapod species (McElwain, Beerling, and Woodward 1999). Emplacement of the CAMP occurred over a relatively short time interval of ~ 1-2 million years (Aarnes et al. 2010; Marzoli et al. 1999). Previous thermodynamic modeling has suggested that the lithologies intruded by an igneous sill may have significantly contributed to the volatiles emitted to the atmosphere

(Aarnes, Fristad, et al. 2011). However, direct geochemical investigations that constrain the quantity of volatiles evolved from CAMP host rocks have not been conducted.

Geochemical, petrographic, thermal and thermodynamic data are presented here, focusing on variations in carbon, sulfur and iron within individual sedimentary beds that are cross-cut by a large dike, intruded as part of the CAMP. Carbon isotopes, total organic carbon (%TOC) content, sulfur isotopes and sulfide content were analyzed in a suite of rocks sampled in a transect perpendicular to the dike margin into the country rock. These geochemical data are combined here with thermal and thermodynamic models to reconstruct the thermal evolution and transformation of carbon and sulfur bearing phases. The amount of iron found in different mineralogical pools (carbonate, oxides, magnetite, and silicate) in the samples was quantified in order to characterize how changes in iron mineralogy may play a role in the evolution of other minerals in the system. Mineralogical and textural changes along the transect were examined through petrographic analysis (SEM and optical microscopy) in order to help understand the geochemical data. These methods are combined to answer how this particular dike of the CAMP interacted with the host rocks as well as to classify the thermal history and sources of the possible volatile release.

ii. Geologic Setting

a. Newark Supergroup and CAMP

The Newark Supergroup represents the sedimentary fill in a series of rift basins that line the present-day east coast of North America (Figure 1). These basins occur from South Carolina to Nova Scotia, ranging in age from the Late Triassic (Carnian) through the Early Jurassic (Pliensbachian) (Smoot 1991; Cornet 1977). At the time of deposition, the basins were located near the equator (Olsen 1997). Many of the southern basins are half-grabens with

normal faults defining their western boundaries where the northern basins are bounded by normal faults to the east (Schlische and Olsen 1990). The basins range in size from a few km^2 to larger than 7500 km^2 and have been filled with alluvial, fluvial and lacustrine deposits (Smoot 1991). The basins within the Newark Supergroup contain cyclic deposits that have been linked to climatic variations due to Milankovitch cyclicity which controlled lake levels at the time of deposition (Olsen 1986).

Many of the basins in the Newark Supergroup have been intruded by diabase dikes and sills of the Central Atlantic Magmatic Province (CAMP) (Smoot 1991). CAMP extends more than 10^7 km^2 over North America, South America, Europe and Africa. Along the eastern United States the CAMP initiated in the north and progressed south, with peak volcanic activity at ~201 Ma, coincident with the T-J boundary (Marzoli et al. 2004; Marzoli et al. 1999; Marzoli et al. 2011; Blackburn et al. 2013). This study particularly focuses on a CAMP dike which has intruded into the Culpeper Basin.

b. Culpeper Basin

The Culpeper Basin lies in the southern half of the extent of Newark Supergroup and occurs in both present day northern Virginia and Maryland (Figure 1). Like many other basins in the Newark Supergroup it is an elongate half graben that is bounded to the west by eastward dipping normal faults. The western border faults separate the Mesozoic basin fill from the Precambrian rocks of the Blue Ridge Province, while on the eastern basin boundary the sedimentary fill laps onto the Appalachian Piedmont Province. It has been suggested that the Culpeper and the adjacent Gettysburg and Newark Basins to the north were all hydrographically connected during deposition of the Newark Supergroup; this is based on the similar stratigraphy in the basins and the orientation of their master faults (Olsen, Gore, and

Schlische 1989). In the northern section of the Culpeper Basin, where my field site is located, the Newark Supergroup consists of at least three distinct formations ranging in age from Carnian to Late Hettangian (Lee 1977; Olsen, Gore, and Schlische 1989; Cornet 1977). The lowest stratigraphic unit of the Culpeper Basin consists of the Manassas Sandstone Formation (Late Triassic) which is comprised of fluvial sandstones and conglomerates with a thickness ranging from ~346 to 1,422 meters (Lee 1977). The Manassas Sandstone is overlain by the Balls Bluff Siltstone Formation (Late Triassic), named after the Balls Bluff National Cemetery in Loudoun County and consists of lacustrine shales, siltstones, sandstones and limestones with a combined thickness of ~95 to 2,190 meters (Lee 1977). This formation is the sedimentary target of this study. The Bull Run Formation (Late Triassic to Early Jurassic) lies above the Balls Bluff and tops off the sedimentary sequence of the Culpeper Basin. This formation consists of fluvial conglomerates and clastics, containing three sequences of basaltic flows, and ranges in thickness up to 5,100 m (Gore 1988; Lindholm 1979). The Rapidan sill of the CAMP intruded the Culpeper Basin around the time of peak magmatic activity of the LIP (200.8 ±1.3 to 201.6 ±1.5 Ma) (Marzoli et al. 2011). The interaction of a single large (>150 m width) dike emanating from the Rapidan sill with the sedimentary rocks of the Balls Bluff Siltstone is the subject of this study.

2. Methods

i. *Sample collection and preparation*

Samples were collected at the Luck Stone Fairfax Quarry (38º49’48.8”N, 77º29’24.2”W) just outside of Centreville, Virginia. 40 samples were collected on the half meter to meter scale

interval within single beds of the Balls Bluff Siltstone with increasing distance from the diabase intrusion. Sampling single beds, cut orthogonally by the dike, was done to minimize potential sedimentary heterogeneity. Samples were collected from three beds of similar facies, consisting of dark brown shale, for a total distance of 21.9 m from the intrusion. The first bed (Bed 1) consisted of 16 samples (FQ-1 to FQ-16) ranging from 0 meters to 7.8 meters from the diabase. The second bed (Bed 2) was 80 centimeters above Bed 1 in a similar lithofacies and consisted of 13 samples (FQ-17 to FQ-29) ranging from 7.8 meters to 15.9 meters from the intrusion. In the third bed (Bed 3: 50 centimeters up stratigraphically from Bed 2) 11 samples (FQ-30 to FQ-40) were collected ranging from 15.9 to 21.9 meters from the intrusion. In addition to those 40 samples 4 more samples were collected, one sample of the diabase (FQ-41) itself and 3 samples (FQ-42 to FQ-44) that were ~272-312 meters from the dike (measured in google maps). In total the three beds that were sampled captured a continuous 21.9 meter long interval away from the CAMP dike.

After obtaining our samples each one was cleaned and the weathered portions were removed with a water-cooled rock-saw. 32 samples were selected and cut for the production of thin sections: 12 samples from Bed 1, 13 from Bed 2, 5 from Bed 3, the sample from the diabase, and one from the distal samples. The portions of these samples were sent to Spectrum Petrographics Inc. for standard 27x46 mm microprobe finished thin sections. The remaining pieces of the samples were powdered with a ball mill and homogenized with a mortar and pestle.

An additional set of samples were collected as part of a pilot study that I did as an undergraduate from a separate bed. These 17 samples were analyzed for total organic carbon and $\delta^{13}C_{org}$ and 7 of them were run through the disulfide extraction and sulfur isotopic analysis.

Results from these samples can also be found in the appendix. An estimated distance from the dike was assumed during the collection of these samples since the contact of this bed with the dike had previously been destroyed by quarrying activities.

ii. *Total organic carbon (TOC) contents and organic carbon isotopic composition ($\delta^{13}C_{org}$)*

To analyze each sample for TOC and $\delta^{13}C_{org}$ ~0.3 g of sample powder was acidified in 2 N HCl for 48 hours to eliminate any carbonate minerals in the sample. Following acidification, the samples were rinsed with doubly deionized water until a neutral pH was reached. Samples were then dried in an oven at ~45ºC. Each sample was then homogenized with a mortar and pestle and ~40 mg was loaded into tin capsules for analysis. Samples were analyzed for TOC and $\delta^{13}C_{org}$ using an IsoPrime 100 gas source stable isotope ratio mass spectrometer coupled with an Elementar vario ISOTOPE elemental analyzer. Precision of TOC determined by commercial standards was equal to or better than 14% (1σ). Isotopic compositions are reported in standard delta notation as per mil (‰) deviations relative to the Vienna Pee Dee Beleminite (V-PDB):

$$\delta^{13}C_{org}=\frac{(^{13}C/^{12}C)_{sample}-(^{13}C/^{12}C)_{VPDB}}{(^{13}C/^{12}C)_{VPDB}}x1000$$

International and commercial standards used to calibrate the sample data to the VPDB scale included Elemental Analysis' wheat flour, IAEA CH-6 and CH-7. Precision of analyses was equal to or better than 0.1‰ (1σ).

iii. *Monosulfide, sulfate and disulfide extractions and sulfur isotope composition ($\delta^{34}S$)*

I used a modified version of the sequential methods of Canfield et al. (1986) and Zhabina and Volkov (1978) to extract and quantify sulfur found in monosulfides (pyrrhotite,

chalcopyrite, etc.), sulfates (barite, etc.), and disulfides (pyrite, etc.). The extracted sulfur was then run through the mass spectrometer to analyze the isotopic compositions of each species.

a. *Acid Volatile Sulfide Extraction*

For this extraction ~10 grams of sample were placed in a three-necked flask. 5 grams of tin (II) chloride were added to the flask to prevent the production of Fe^{3+} from the sample and its reaction with the liberated H_2S gas. Then the flasks were attached to the distillation line and purged with nitrogen gas for 10 minutes. After purging the line, 80 mL of 6M HCl were injected into the reaction flask and allowed to react for 20 minutes after which heating mantles beneath the flasks were turned on for 2 hours allowing for the conversion of sulfur in monosulfide minerals in the rock to be liberated as H_2S gas. The H_2S gas that is carried up through a distillation column and bubbled through a trap containing 3% zinc acetate solution. As the H_2S gas bubbles passed through the zinc acetate solution, the sulfide reacted with aqueous zinc to form solid ZnS. After 2 hours, the zinc acetate traps were removed from the distillation line and 5-10 drops of 5% silver nitrate are added to the traps to convert the ZnS to solid Ag_2S precipitate. The remaining sample and HCl solution in the three-necked flask is then used to extract sulfate and disulfides discussed in the next sections.

b. *Sulfate precipitation procedure*

The remaining sample and HCl in the three-necked flask was then filtered with 0.45μm filter paper and the solution was transferred into an Erlenmeyer flask containing 20 mL of 0.7M barium chloride ($BaCl_2$) solution to precipitate dissolved sulfate as barium sulfate ($BaSO_4$). The remaining solid sample on the filter paper dried in an oven in preparation for the disulfide extraction. The $BaSO_4$ precipitate was then filtered, rinsed with doubly deionized water (18 Ω) until the solution reached a neutral pH and then dried.

c. *Chromium Reduction Sulfide Extraction*

The chromium reduction procedure developed by Canfield et al. 1986 is used to extract the remaining sulfides in the rock which includes pyrite and other disulfides. The dried solid sample was placed back in the three-necked reaction flask with 10mL of ethyl alcohol. The flasks were then attached to a distillation line and purged with nitrogen gas for 10 minutes. After purging, 40 mL of 1M chromium chloride and 20 mL of 12M HCl were injected into the reaction flask. The samples were then left to react for 20 minutes after which the heating mantles were then turned on for 2 hours allowing for the release of H_2S gas. The H_2S flows through a distillation column into the zinc acetate trap solution as described above for the monosulfide extraction. After the extraction was completed 5 to 10 drops of 5% silver nitrate was added to form solid Ag_2S, also as described above.

d. *Sulfur Isotopic analysis*

To analyze the isotopic composition of the sulfur minerals present, ~0.3 - 0.4 mg of the extracted precipitates was weighed out and placed into a tin capsule. V_2O_5 is added to the sample to ensure complete combustion of the sample and conversion to SO_2 gas. The sample was then analyzed on an Elementar vario ISOTOPE elemental analyzer coupled to an IsoPrime 100 gas source stable isotope ratio mass spectrometer. Sulfur isotope compositions are reported in delta notation ($\delta^{34}S$), as defined for carbon above, with comparison to the Vienna Cañon Diablo Troilite (V-CDT and reported as per mil (‰) with a precision of < 0.2 ‰ (1σ).

iv. *Iron Speciation*

a. *Sequential Extraction*

Iron speciation analyses were conducted following the sequential method of Poulton and Canfield (2005). This method quantifies the amount of iron that resides in the carbonate, oxide (excluding magnetite), and magnetite minerals within the sample. In this procedure ~0.2 g of powdered sample was placed into 15 mL centrifuge tubes. The first step in the sequential extraction is to extract the iron that is in carbonate minerals, including siderite, ankerite and dolomite. For this step, 10 mL of 1M solution of sodium acetate that was buffered with acetic acid to a pH of 4.5 was added to the centrifuge tubes with the sample and placed on a heated shaker table for 48 hrs at 50ºC. After this step was completed, the samples and solution were then centrifuged and 100 μL of solution was taken from each sample for quantification of its iron contents following the procedure described below. The remaining solution in the sample tube was then discarded leaving just the remaining sample in the tube.

The second step in the extraction releases iron trapped in oxide minerals such as goethite and hematite but not magnetite. This step used a 50 gL^{-1} sodium dithionite solution buffered to a pH of 4.8 with both acetic acid and sodium citrate. 10 mL of sodium dithionate solution was added to the sample and placed on a shaker table for 2 hours. Following the 2 hours, the same steps mentioned below were taken to measure the iron content. The final extraction in the sequence is used to release iron that is trapped in magnetite. 10 mL of 0.2 M ammonium oxalate buffered to a pH of 3.2 is added to the remaining sample and places on a shaker table for 6 hours. After the time has elapsed the steps outlined below to measure the iron content are followed.

b. Total Iron content

To determine total iron contents ~0.2-0.3 g of sample powder was weighed out into ceramic crucibles and were heated in a furnace at 900˚C for 8 hours in order to remove volatile phases

such as organic matter. The remaining ashed sample was then weighed and homogenized with a mortar and pestle. ~0.08 g of the ashed sample was then weighed out and placed into a Teflon bomb with 4mL of concentrated (12M) HCl. These bombs were then heated on a hot plate at 140-145˚C for 48 hours. This step released the iron in the sample into solution. After heating, the solution and residuum were rinsed into a 50 mL centrifuge tube, which was then filled to the 50 mL line for dilution. Iron content was determined by the method described below.

c. Iron content measurement

Following each iron extraction a 100 μL aliquot was taken off of the top of the solution and combined with 4 mL of a ferrozine solution with the addition of hydroxylamine HCl. The addition of reducing agent hydroxylamine HCl ensures the conversion of all the aqueous iron to ferrous iron (Fe^{+2}). The iron contents of each solution was determined in wt% by using the ferrozine spectrophotometer method (Stookey 1970; Viollier et al. 2000). Replicate analyses of these analyses yielded a precision equal to or better than 4.0% (1σ).

v. *Petrographic analysis*

a. *Optical Microscopy*

A Nikon Optihot-Pol reflected and transmitted light microscope was used to locate and describe the minerals and textures present in each thin sectioned sample. Transmitted light thin sections were examined to determine mineralogical compositions such as plagioclase, clays and possible iron oxides and sulfides, as well as, grain size distributions and textures in each sample. Under reflected light, iron oxide and sulfide minerals were identified and size, shape and distribution were noted.

b. *Scanning electron microscope (SEM) analysis*

Thin sections of the samples were carbon coated and analyzed on the CamScan Series II Scanning Electron Microscope to obtain back scatter electron images and mineral spectra. Images and several spectra were taken from each thin section in order to identify mineralogy in the samples, particularly the sulfide and iron oxide minerals. Once iron oxide minerals were located they were then examined under reflected light to distinguish between magnetite and hematite. Spectra transects were made across mineral grains in order to identify coexisting phases and different intervals of crystal growth.

3. Results

The results discussed in this section will only be those from Bed 1, which is the only transect that displays clear alteration from the dike. Additionally, sulfate content and isotopic composition will not be discussed because the extractions yielded no measurable sulfate from the samples. Results for the other two beds (Beds 2 and 3) that were sampled and analyzed can be found in the appendix.

i. Carbon geochemistry

Total organic carbon (TOC) content along Bed 1 is variably low containing a range between 0.04 and 0.05 wt% (Figure 2). There is minimal change in the TOC along this bed; the difference between the sample at the contact with the intrusion to the sample at the end of the bed (7.8 meters from the intrusion) is 0.01 wt%.

Carbon isotopic values along bed 1 range from -29.27 to -28.64‰. Isotopic values become more negative with distance from the intrusion: the sample most proximal to the intrusion has

an isotopic value of -28.83‰ while the most distal sample along this bed hold an isotopic value of -29.25‰ with a total change of 0.42‰ (Figure 3).

ii. Sulfur geochemistry

Monosulfide content along Bed 1 ranges between 0 and 565 ppm with the final sample in the bed containing the highest value. Samples more proximal to the intrusion contain values on the order of 10 ppm while the samples in the middle of the transect drop down to values around 1 ppm (Figure 4; zero value is not pictured because the y-axis is in log scale). Disulfide content along bed 1 ranges between 37 and 773 ppm with the highest value occurring at the last sample while the rest of the transect varies on the order of 10 ppm (Figure 5).

Monosulfide isotopic values of Bed 1 range between -22.76 and -2.84‰ (Figure 6). The least negative values occur near the dike, which has a monosulfide isotopic value of 1.2‰, and away from the dike the values become more negative until sample FQ-12 (5.8 meters from the intrusion) where the values then start to become less negative up to the last sample in the bed at -9.6‰ this pattern resembles an asymmetric v-shape. Disulfide isotopic values range between -10.23 and 4.50‰ (Figure 7) where the more positive values are proximal to the dike, with a value of 1.0‰, and the most negative value, -10.2‰, is in the last sample of Bed 1.

iii. Iron geochemistry

Iron carbonate contents (Fe_{carb}) along Bed 1 ranges between 0.08 and 0.28 wt%, where the trend is generally flat except for the last sample in the bed which contains the highest value found in the bed. Fe_{carb} in the diabase dike is 0.33 wt%; since this is a sample of igneous rock it is potentially a measure of iron in a different phase other than siderite or dolomite such as pyroaurite (Table 1). Iron oxide in Bed 1 ranges between 0.02 and 0.47 wt% Fe_{ox} (Table 1) while the diabase has a Fe_{ox} value of 0.04 wt%. Magnetite content (Fe_{mag}) for Bed 1 ranges

between 0.70 and 1.22 wt% with the highest values closest to the intrusion and decreasing with distance with the exception of FQ-16 which has a Fe_{mag} value of 1.22 wt% (Figure 8). The diabase has a Fe_{mag} content of 0.72 wt% (Figure 8). Silicate iron or unreactive iron (Fe_{ur}) makes up the largest pool of iron seen in the transect. Bed 1 contains a range from 2.06 to 3.76 wt% Fe_{ur}. Unreactive iron across the transect is generally flat (Table 1). Overall the respective iron phases consisting of iron oxide and iron carbonate are quantitatively less significant compared to the iron found in magnetite and unreactive iron.

iv. Petrographic results

Optical microscopy of thin sections along bed 1 (Figure 9) showed textural changes along the transect. Along the transect the samples are relatively the same in regard to grain size, sorting, and color except for the last sample of the transect. FQ-1 and FQ-3, which are proximal to the contact with the diabase, consist of mainly clay sized mineral grains (smaller than 2μm) with a few larger grains (~2 mm) of plagioclase and quartz. Both samples exhibit some wavy textures that may be due to post depositional fluid flow (Figure 9). Samples FQ-4 and FQ-6 are dominated by a clay sized matrix with some larger grains (< 1%) also containing the whispy textures indicating possible fluid flow in this sample. In addition, FQ-6 contains opaque minerals that look like magnetite in reflected light, these grains are very broken up and resemble skeletal magnetite. Samples FQ-7 through FQ-11 contain well-sorted clay sized grains with magnetite (opaque mineral) disseminated throughout the sections. FQ- 13 also consists of clay sized grains with magnetite distributed throughout the section. In addition there is the presence of magnetite within the veins. Sample FQ-14 consists of clay sized grains but exhibits very little to no magnetite. Sample FQ-16 contains a color gradient from tan to black

with grains ranging from clay to sand sized. The larger grains in this sample consist of magnetite, chalcopyrite and pyrite.

SEM analysis revealed iron-titanium oxide minerals, such as magnetite and ilmenite, in samples FQ-1 to FQ-11. Sample FQ-1 contained barite and chalcocite but the rest of the samples from FQ-2 to FQ-10 exhibited no visible sulfides or sulfates, although sample FQ-7 contained a copper-zinc-nickel alloy. Chalcopyrite, was found in sample FQ-13 occurring within a quartz grain and had a grain size of less than 10 μm. Sample FQ-14 contained larger chalcopyrite grains (~25 μm) and native copper. Analysis of sample FQ-16 found very large sulfides (pyrite and chalcopyrite) (> 100 μm) occurring with magnetite. Images of the minerals in the samples mentioned above can be found in Figure 10.

v. Thermal modeling

Thermal models were constructed in one dimension and two dimensions (Figure 11 and Figure 12a) to examine the potential size of the contact aureole using a finite difference method taken from Spear (1993). This method is used to solve a one-dimensional diffusion equation:

$$\frac{dT}{dt} = \kappa(\frac{\partial^2 T}{\partial x^2})$$

where, *T* is temperature, *t* is time, κ is thermal diffusivity (calculated below) and *x* is distance. The calculation for thermal diffusivity is defined as:

$$\kappa = \frac{k}{c\rho}$$

where k is thermal conductivity, c is specific heat capacity and ρ is density. In the construction of these models, a dike thickness of 170 meters is used (measurement taken from field photo), along with an assumed initial dike temperature of 1200ºC and the initial temperature of the

sediments of 70ºC, following the geothermal gradient proposed by Malinconico (2002). Both models used a country rock density of 2640 kg/m^3 as calculated below, a thermal conductivity of 1.6 W/mK and a specific heat capacity of 870 J/kgK (Eppelbaum, Kutasov, and Pilchin 2014; Clark 1966; Blackwell and Steele 1989). Both thermal models show a thermal aureole extending ~ 315 meters from the dike, in which temperatures are considerably elevated above the initial condition of 70ºC. Temperatures of the country rock at the contact reach a maximum of just under 600ºC, rapidly decreasing with distance from the intrusion. Additional models in one-dimension were done to examine the maximum temperature reached in x-space (Figure 12b) and a model of the number of years a certain rock experiences temperatures above 300 and 150 (Figure 12c). These models, and many similar examples in the literature, imply heating of sedimentary rocks far outside the contact aureole observed in the field. The observable isotopic and textural changes associated with dike emplacement extend less than 10 m from the dike rather than the tens to hundreds of meters predicted in the thermal model. Two main reasons could account for this: (i) the simple modeling neglects heat advection in fluids and is thus fundamentally inappropriate for understanding the system of interest, (ii) the thermal model is, to a first order, appropriate but most rocks in the sequence did not respond mineralogically and geochemically to the short pulse of heating that they experienced. It is likely that this second possibility, kinetic inhibition to recrystallization, is particularly important.

4. Discussion

i. Alteration of carbon isotope composition of sedimentary organic matter associated with dike emplacement

Previous studies have suggested thermogenic methane can be produced by heat from igneous bodies that intrude into organic-rich sediments (Yallup, Edmonds, and Turchyn 2013; Aarnes et al. 2010; Yoksoulian 2010; Svensen et al. 2004). In this study, the isotopic composition of the organic carbon along the transect shows an enrichment of $\delta^{13}C$ approaching the intrusion (Figure 3). This pattern in other studies is suggestive of the production of thermogenic methane proximal to the intrusion, which is known to be more enriched in ^{12}C (Sackett, Nakaparksin, and Dalrymple 1970) with values ranging between -35 to -50‰ (Svensen et al. 2004). The changes seen in the carbon isotopic values are not reflected in the TOC content, where a loss in organic carbon would be expected proximal to the intrusion. In order to test whether the production of thermogenic methane could occur without a discernable decrease in TOC content (greater than 0.1 wt%. Figure 2), but alter the organic carbon isotopic composition of the sediments, I used a two component mixing model (Faure and Mensing 2005) to determine the amount of carbon that could be lost as thermogenic methane:

$$\delta^{13}C_m = \delta^{13}C_f f + \delta^{13}C_{CH4}(1 - f)$$

where C_m is the original isotopic composition of the sedimentary organic carbon before heating, C_f is the isotopic composition of the rock after methane production and release, $\delta^{13}C_{CH4}$ is the isotopic composition of the thermogenic methane that was produced and f is the fraction of remaining carbon in the rock after the release of thermogenic methane. Using this mixing model, the measured isotopic compositions and the range of isotopic compositions for thermogenic methane (Schoell 1984; Svensen et al. 2004), the fraction of organic carbon remaining varies between 86 and 96%. This is broadly consistent with the observation of a lack of measurable change in the measured TOC content along the transect.

From the isotopic mixing model we can calculate the amount of carbon released through the production of thermogenic methane; using a density of 2.64 g/cm^3 which was calculated by massing a rock (sample FQ-9 arbitrarily chosen) in the transect and then measuring its volume by observing how much water it displaced in a graduated cylinder. This number falls within the range of densities reported for siltstones and shales (Birch and Clark 1940; Ferti and Atlas 1980; Yallup, Edmonds, and Turchyn 2013; Spear 1993; Ho et al. 1989). The amount of carbon released with the production of thermogenic methane can be calculated by first taking the density and converting it to grams per meter cubed and then multiplying that by the averaged wt% TOC within the transect. This number is then multiplied by the ranges of the percent of carbon leaving the rock through thermogenic methane production based on the wt% of organic carbon remaining reported above. This calculation gives estimates of the amount of thermogenic methane loss per rock volume between 51 g to 177 g of C per m^3. This occurs within the first meter from the intrusion. Although the production of thermogenic methane most likely occurred at a wider range than 1 meter it may have not been able to escape due to permeability constraints. Given these results, the production of thermogenic methane seems to be a likely mechanism controlling the organic carbon isotopic signature seen in Figure 3.

The addition of carbon from magmatic fluids is also a possible mechanism to explain the change in organic carbon isotope composition of the altered siltstone. Using a slightly different mixing model and the isotopic signature expected for mantle CO_2 (-5 to -7‰; Gerlach and Taylor 1990)

$$\delta^{13}C_m = \delta^{13}C_a f + \delta^{13}C_{CO2}(1-f)$$

where C_m is the mixed isotopic composition of the mantle derived CO_2 and the original organic carbon in the sediments, C_a is the isotopic composition before the addition of mantle

CO_2 and $\delta^{13}C_{CO2}$ is the isotopic composition of carbon in mantle derived CO_2. The amount of carbon assimilated into the country rock would be around 4% of the total organic carbon seen proximal to the intrusion, allowing for 96% of the original organic carbon in the sediments to remain. Although this is a possible mechanism for the trend seen in both the TOC and $\delta^{13}C_{org}$ no graphite is seen within the thin sections in transmitted or reflected light, which would give textural evidence for the addition of carbon derived from the melt. There may have been a possible exchange of carbon from magmatic CO_2 with the organics in the rock but if so it was minimal because the mantle carbon signature only makes up 4% of the entire signature. The possibility of carbon from mantle derived CO_2 being reduced and incorporated into the country rock as phases other than carbonate minerals is unlikely at the estimated pressures and temperature present during emplacement of the intrusion (Lowenstern 2001).

Additional analyses would be useful for determining which mechanism controlled the isotopic signature seen along the transect. These include vitrinite reflectance, X-ray Diffraction and isotopic analysis of the carbonate minerals in the rock. The vitrinite reflectance analysis would allow for the examination of the maturity of the organic matter within the sediments and how it changed relative to the dike intrusion. X-ray diffraction (XRD) of bulk rock would allow for the identification of any graphite. This method would also allow for the characterization of fluid precipitated graphite based on the different crystallinity seen in the XRD spectra (Luque et al. 1998). Lastly the isotopic composition of the carbonate minerals may give insight to whether or not CO_2 from the mantle was assimilated into the sediments as carbonate instead of graphite.

ii. Alteration of the sulfur system during dike emplacement

Previous studies of magmatic copper-nickel and platinum group element deposits and similar environments have suggested that sulfur from country rock can be assimilated into the intruding magmas and that much of this sulfur is eventually lost to the atmosphere through degassing (Ripley and Li 2003; Power, Pirrie, and Andersen 2003; Yallup, Edmonds, and Turchyn 2013). However, there are elevated sulfide contents at the beginning and the end of the Bed 1 transect (Figures 4 and 5) and this sulfide has sulfur isotopic compositions that are in the range of magmatic sulfur (Figures 6 and 7). Moving away from intrusion, sulfide contents and $\delta^{34}S$ decline reaching a low between 5 and 6 meters and the lowest $\delta^{34}S$ values reached are indicative of sulfide produced from microbial sulfate reduction. Copper sulfide minerals also occur at each end of the transect as well as elevated magnetite contents. With these patterns in mind, I hypothesize that sulfur and copper were sequestered into the siltstone from the magma and that the thermal break down of sedimentary pyrite occurred but that the majority of the liberated sulfur was retained in the country rock. (Figure 13). This hypothesis is explored further and tested below.

The thermal decomposition of pyrite and the presence of both higher magnetite and copper sulfide minerals at either end of the transect can be explained by reactions discussed by Toulmin et al (1964), Tomkins (2010), and Yallup et al, (2013) and Elliot and Watling (2011):

$$FeS_2 \rightarrow Fe_{(1-x)}S + \frac{1}{2}\,S_2$$

This equation represents the simple breakdown of pyrite thermally to pyrrhotite with the liberation of a sulfur species. Pyrrhotite was not observed in the transect, however copper sulfides and native copper are present. Pyrrhotite can be converted to chalcopyrite in the

presence of copper rich fluids by reactions proposed by Elliot et al., (2011) where pyrrhotite reacts to form the unnamed mineral ($CuFe_3S_4$), isocubanite, and finally chalcopyrite:

$$3Fe_7S_8 + 9Cu^{2+} \rightarrow 8CuFeS_2 + CuFe_7S_8 + 6Fe^{3+}$$

$$CuFe_7S_8 + Cu^{2+} \rightarrow 2CuFe_3S_4 + Fe^{2+}$$

$$3CuFe_3S_4 + Cu^{2+} \rightarrow 4CuFe_2S_3 + Fe^{2+}$$

$$2CuFe_2S_3 + Cu^{2+} \rightarrow 3CuFeS_2 + Fe^{2+}$$

These reactions are just examples of the formation of chalcopyrite from pyrrhotite and Cu^{2+}, but chalcopyrite can be produced with reactions of pyrrhotite with Cu^{+} and Cu^{0} as well. During these reactions there is a release of both ferric and ferrous iron which would allow for the formation of magnetite (Fe_3O_4); this would explain the elevated magnetite contents observed proximal to the intrusion and at the distal end of the transect.

To better understand the observed coexistence of pyrite, chalcopyrite and magnetite in the last sample of the transect, simple thermodynamic models of the stability fields of these phases were calculated as a function of sulfur and oxygen fugacities for temperatures ranging from 100 to 600ºC at 0.5 kbars (Figure 14a, b, c, and d). The simplicity of these models comes from the fact that only three different types of fluid can be generated (H_2, H_2O and H_2S) and there is no dissolution of any mineral into a water dominated fluid. These models used a SiO_2, Cu, Fe, H, O system and made calculations through the program Perple_X (Connolly 2005) using Gibbs free energy minimization and end-member data for silicates, oxides and sulfides from thermodynamic a data file called: ctransf (Helgeson et al. 1978 and references therein). The model results show that there is no field in which pyrite, chalcopyrite, and magnetite can exist as a stable mineral assemblage, suggesting that pyrite occurs as a secondary phase, partly replacing a chalcopyrite + magnetite-bearing assemblage. This is supported by the

petrographic observations: euhedral pyrite coexists with chalcopyrite and magnetite that display decomposition textures (Figure 10g).

In order to interpret the sulfide isotopic composition seen along the transect a simple two component mixing model (Faure and Mensing 2005) is used with the assumption that the decomposition of pyrite causes very little (< 1‰) fractionation (Yamamoto 1984). We can determine the fraction of sulfur that was added from the dike into the sediments:

$$\delta^{34}S_m = \delta^{34}S_{sed}f + \delta^{34}S_{int}(1-f)$$

where $\delta^{34}S_m$ is the mix of sedimentary sulfur and magmatic sulfide, $\delta^{34}S_{sed}$ is the initial composition of the sedimentary sulfide, *f* is the fraction of sedimentary sulfide in the mixture and $\delta^{34}S_{int}$ is the sulfide isotopic composition of the dike. If we calculate *f* for the side of the v (Figure 6) that contacts the dike using 1.2‰ as $\delta^{34}S_{int}$, -13.0‰ as $\delta^{34}S_m$ (the average for the area that represents a mixed isotopic composition. i.e. between 2.8 and 3.3 meters from the intrusion) and -22.7‰ as $\delta^{34}S_{sed}$ assuming this represents the background sedimentary sulfide. Using these values, a value of 0.59 is calculated for *f*, meaning these samples reflect a mixture of 59% sedimentary sulfide and 41% magmatic sulfide. If we calculate the amount of S added to the monosulfide sulfur pool using the average concentration of monosulfide sulfur in these samples, 6 ppm S of magmatic sulfide was added to the sedimentary rocks. The samples closer to the intrusion reflect a higher contribution of magmatic sulfur (~20 ppm S or 24% magmatic sulfur). The sulfur isotopic signature at the end of the transect is similar to that of the mixed area seen closer to the intrusion (end of transect $\delta^{34}S$: -9.6‰) which is attributed to the addition of sulfur from magmatic fluids. This suggests that the path of the fluid flow from the intrusion may to have come from the dike and into the adjacent beds but then reached an area of lower permeability and was forced to flow elsewhere. Fluid flow was then allowed to return to that

bed in the distal samples possibly due to faulting or fracturing (Figure 15). Alternatively, the alteration that occurs at the end of the bed may be due to fluid flowing from the intrusion through localized fractures that cut bedding (Figure 15); however large-scale fractures in this part of the transect were not observed in the field .

Disulfide shows a similar pattern in isotopic composition and content to the monosulfides over the transect, however this data set is much more limited due to the low disulfide abundances in the samples. The isotopic compositions of the samples proximal to the intrusion is consistent with addition of magmatic sulfur to the siltstone. The disulfide sulfur isotopic composition at the end of the transect is similar to the monosulfide sulfur isotopic composition at the end of the transect which could indicate a closed system behavior of the sulfur isotope systematic meaning sulfur in the euhedral pyrite observed in these samples could have been derived from sulfur liberated from the breakdown of chalcopyrite.

Additional work that would help further constrain the processes behind the observed geochemical and mineralogical trend include secondary ion mass spectrometry (SIMS), where the isotopic composition of individual grains and changes in isotopic composition within a single grain could be measured. Another useful method to look at sulfides and their transformations within this bed would be the use of a microprobe to map the composition across grains of chalcopyrite to examine possible changes in copper and iron content from the rim to core, which could reflect the reactions that converted pyrrhotite to chalcopyrite.

5. Conclusions

Integrated analyses of both geochemical and petrographic data have revealed fluid-driven thermal reactions within the carbon and sulfur species in both the country rock and magmatic

intrusion. Broadly, the observed mineralogical and geochemical changes occur in a much narrower zone adjacent to the intrusion than predicted by the thermal model and suggest that kinetic limitations played an important role in the type and extent of alteration that the sedimentary rocks experienced. The release of 50 to 177 g/m^3 of C in thermogenic methane from the sedimentary rocks proximal to the intrusion is exhibited through isotopic analyses of organic carbon where $\delta^{13}C$ becomes enriched as the dike is approached. Additionally, the sequestering of magmatic sulfur into the country rock and its mixing with biogenic derived sulfur from the breakdown of sedimentary sulfides is reflected within sulfide content and its isotopic composition in the siltstone. The thermal breakdown of sedimentary pyrite to pyrrhotite and its conversion to chalcopyrite with the addition of sulfur from the dike is hypothesized as a mechanism for the mixed isotopic signatures along the transect. These data suggest an incorporation of magmatic sulfur into this particular sedimentary bed and conservation of the local sedimentary sulfur.

This study has yielded further insights into the chemical and mineralogical changes due to thermal alteration of sedimentary minerals and their evolution within the contact metamorphic environment. The study highlights the importance of the initial composition of the country rocks on the volatile budgets of the overall magmatic-contact-metamorphic system. Specifically, heterogeneity of sedimentary rocks at the scale of single beds can affect the quantities and species of carbon and sulfur liberated from or lost from the magmatic system. Moreover, models for the alteration of country rock need to account for kinetic limits on contact metamorphic reactions, which can drastically limit the zone of alteration around the intrusion. The hypothesized role of volatiles released from the sediments that have been intruded by LIPs, which is on the order of 10s to 100s of kg/m^3 of methane (Aarnes et al. 2010),

in pushing climate perturbations as a mechanism for mass extinction events throughout the Phanerozoic may need to be reevaluated potentially using data from this study, where the volatiles released are orders of magnitudes smaller. Additional work should be done in collaboration with modelers like the Aarnes group in order to scale down the role of the host rock based on data from actual rocks instead of assumptions made by modelers without rocks.

References

Aarnes, Ingrid, Kirsten Fristad, Sverre Planke, and Henrik H. Svensen. 2011. "The Impact of Host-Rock Composition on Devolatilization of Sedimentary Rocks during Contact Metamorphism around Mafic Sheet Intrusions." *Geochemistry, Geophysics, Geosystems* 12 (10). doi:10.1029/2011GC003636.

Aarnes, Ingrid, Henrik H. Svensen, James A D Connolly, and Yuri Y. Podladchikov. 2010. "How Contact Metamorphism Can Trigger Global Climate Changes: Modeling Gas Generation around Igneous Sills in Sedimentary Basins." *Geochimica et Cosmochimica Acta* 74 (24): 7179–95. doi:10.1016/j.gca.2010.09.011.

Aarnes, Ingrid, Henrik H. Svensen, Stephane Polteau, and Sverre Planke. 2011. "Contact Metamorphic Devolatilization of Shales in the Karoo Basin, South Africa, and the Effects of Multiple Sill Intrusions." *Chemical Geology* 281 (3–4): 181–94. doi:10.1016/j.chemgeo.2010.12.007.

Agirrezabala, Luis M., Albert Permanyer, Isabel Suárez-Ruiz, and Carmen Dorronsoro. 2014. "Contact Metamorphism of Organic-Rich Mudstones and Carbon Release around a Magmatic Sill in the Basque-Cantabrian Basin, Western Pyrenees." *Organic Geochemistry* 69: 26–35. doi:10.1016/j.orggeochem.2014.01.014.

Amrani, Alon, Michael D. Lewan, and Zeev Aizenshtat. 2005. "Stable Sulfur Isotope Partitioning during Simulated Petroleum Formation as Determined by Hydrous Pyrolysis of Ghareb Limestone, Israel." *Geochimica et Cosmochimica Acta* 69 (22): 5317–31. doi:10.1016/j.gca.2005.06.026.

Andrews, Mark S., and Edward M. Ripley. 1989. "Mass Transfer and Sulfur Fixation in the Contact Aureole of the Duluth Complex, Dunka Road Cu-Ni Deposit, Minnesota." *Canadian Mineralogist* 27 pt 2: 293–310.

Birch, Francis, and Harry Clark. 1940. "The Thermal Conductivity of Rocks and Its Dependence upon Temperature and Composition." *American Journal of Science* 238 (8): 530–58.

Blackburn, T J, P E Olsen, S A Bowring, N M McLean, D V Kent, J Puffer, G McHone, E T Rasbury, and M Et-Touhami. 2013. "Zircon U-Pb Geochronology Links the End-Triassic Extinction with the Central Atlantic Magmatic Province." *Science* 340 (6135): 941–45. doi:10.1126/science.1234204.

Blackwell, David D, and John L Steele. 1989. "Thermal Conductivity of Sedimentary Rocks : Measurement and Significance." In *Thermal History of Sedimentary Basins*, edited by ND Naeser and TH (eds) McCulloch, 5–96. New York: Springer.

Canfield, Donald E., Robert Raiswell, Joseph T. Westrich, Christopher M. Reaves, and Robert A. Berner. 1986. "The Use of Chromium Reduction in the Analysis of Reduced Inorganic Sulfur in Sediments and Shales." *Chemical Geology* 54: 149–55.

Clark, S.P. Jr. (Ed). 1966. "Handbook of Physical Constants (Revised Edition)." *Geological Society of America*.

Connolly, J A D. 2005. "Computation of Phase Equilibria by Linear Programming : A Tool for

Geodynamic Modeling and Its Application to Subduction Zone Decarbonation." *Earth and Planetary Science Letters* 236: 524–41. doi:10.1016/j.epsl.2005.04.033.

Cooper, Jennifer R., John C. Crelling, Susan M. Rimmer, and Alan G. Whittington. 2007. "Coal Metamorphism by Igneous Intrusion in the Raton Basin, CO and NM: Implications for Generation of Volatiles." *International Journal of Coal Geology* 71 (1 SPEC. ISS.): 15–27. doi:10.1016/j.coal.2006.05.007.

Cornet, Bruce. 1977. "The Palynostratigraphy and Age of the Newark Supergroup." Pennsylvania State University.

Courtillot, Vincent E., and Paul R. Renne. 2003. "On the Ages of Flood Basalt Events." *Comptes Rendus - Geoscience* 335 (1): 113–40. doi:10.1016/S1631-0713(03)00006-3.

Elliot, Alexander Dean, and Helen R Watling. 2011. "Chalcopyrite Formation through the Metathesis of Pyrrhotite with Aqueous Copper." *Geochimica et Cosmochimica Acta* 75 (8). Elsevier Ltd: 2103–18. doi:10.1016/j.gca.2011.01.033.

Eppelbaum, L, I Kutasov, and A Pilchin. 2014. "Thermal Properties of Rocks and Density of Fluids." In *Applied Geothermics*, 99–149. Springer. doi:10.1007/978-3-642-34023-9.

Faure, Gunter, and Teresa M. Mensing. 2005. *Isotopes Principles and Applications*. 3rd ed. John Wiley & Sons Inc.

Ferti, Walter H, and Dresser Atlas. 1980. "Evaluation of Shaly Clastic Reservoir Rocks." *Journal of Petroleum Technology*, no. September: 1641–46.

Gerlach, Terrence M., and Bruce E. Taylor. 1990. "Carbon Isotope Constraints on Degassing of Carbon Dioxide from Kilauea Volcano." *Geochimica et Cosmochimica Acta* 54 (7): 2051–58. doi:10.1016/0016-7037(90)90270-U.

Gore, P. J. W. 1988. "Lacustrine Sequences in an Early Mesozoic Rift Basin: Culpeper Basin, Virginia, USA." *Geological Society, London, Special Publications* 40 (1): 247–78. doi:10.1144/GSL.SP.1988.040.01.21.

Helgeson, Harold C., Joan M. Delany, H. Wayne Nesbitt, and Dennis K. Bird. 1978. "Summary and Critique of the Thermodynamic Properties of Rock-Forming Minerals." *American Journal of Science* 278–A: iii-229.

Hesselbo, Stephen P, S a Robinson, F Surlyk, and S Piasecki. 2002. "Terrestrial and Marine Mass Extinction at the Triassic/Jurassic Boundary Synchronized with Initiation of Massive Volcanism." *3. Annual Meeting of the Palaeontological Association*, no. 3: 19. doi:10.1130/0091-7613(2002)030<0251.

Ho, C. Y., Y. S Touloukian, W. R. Judd, and R. F. Roy, eds. 1989. "Physical Properties of Rocks and Minerals." Hemisphere publishing corporation.

Hu, Guilin, Kim Dam-Johansen, Stig Wedel, and Jens Peter Hansen. 2006. "Decomposition and Oxidation of Pyrite." *Progress in Energy and Combustion Science* 32 (3): 295–314. doi:10.1016/j.pecs.2005.11.004.

Lee, Kwang Yuan. 1977. "Triassic Stratigraphy in the Northern Part of the Culpeper Basin,

Virginia and Maryland." *Contributions to Stratigraphy*, iii, 17 .

Lindholm, R. C. 1979. "Geologic History and Stratigraphy of the Triassic-Jurassic Culpeper Basin, Virginia." *Bulletin of the Geological Society of America* 90 (11 PART II): 1702–36. doi:10.1130/GSAB-P2-90-1702.

Lowenstern, Jacob B. 2001. "Carbon Dioxide in Magmas and Implications for Hydrothermal Systems." *Mineralium Deposita* 36: 490–502. doi:10.1007/s001260100185.

Luque, F J, J D Pasteris, B Wopenka, M Rodas, and J F Barrenechea. 1998. "MINERALOGICAL CHARACTERISTICS AND MECHANISMS OF FORMATION Graphite Commonly Occurs in Metasedimentary Rocks as a Result of the Conversion of Organic Matter through Regional or Contact Metamorphism . From Diagenesis to the Uppermost Metamorphic Grades , Th." *American Journal of Science* 298 (1): 471–98.

Malinconico, MaryAnn Love. 2002. "Lacustrine Organic Sedimentation, Organic Metamorphism and Thermal History of Selected Early Mesozoic Newark Supergroup Basins, Eastern U.S.A." *University of Columbia Dissertation*. doi:10.16953/deusbed.74839.

Marzoli, Andrea, Hervé Bertrand, Kim B. Knight, Simonetta Cirilli, Nicoletta Buratti, Chrystéle Vérati, Sébastien Nomade, et al. 2004. "Synchrony of the Central Atlantic Magmatic Province and the Triassic-Jurassic Boundary Climatic and Biotic Crisis." *Geology* 32 (11): 973–76. doi:10.1130/G20652.1.

Marzoli, Andrea, Fred Jourdan, John H. Puffer, Tiberio Cuppone, Lawrence H. Tanner, Robert E. Weems, Hervé Bertrand, Simonetta Cirilli, Giuliano Bellieni, and Angelo De Min. 2011. "Timing and Duration of the Central Atlantic Magmatic Province in the Newark and Culpeper Basins, Eastern U.S.A." *Lithos* 122 (3–4): 175–88. doi:10.1016/j.lithos.2010.12.013.

Marzoli, Andrea, Paul R. Renne, Enzo M. Piccirillo, Marcia Ernesto, Giuliano Bellieni, and Angelo De Min. 1999. "Extensive 200-Million-Year-Old Continental Flood Basalts of the Central Atlantic Magmatic Province." *Science* 284: 616–18. doi:10.2113/gselements.1.5.293.

McElwain, J., D. Beerling, and F. Woodward. 1999. "Fossil Plants and Global Warming at the Triassic-Jurassic Boundary." *Science* 285 (AUGUST): 1386–90. http://www.jstor.org.libezproxy.open.ac.uk/stable/2898784?seq=1#page_scan_tab_contents.

Olsen, Paul E. 1986. "A 40-Million-Year Lake Record of Early Mesozoic Orbiatal Climatic Forcing." *Science* 234 (November 14, 1986): 842–48.

Olsen, Paul E. 1997. "Stratigraphic Record of the Early Mesozoic Breakup of Pangea in the Laurasia-Gondwana Rift System." *Annual Review of Earth and Planetary Sciences* 25 (1): 337–401. doi:10.1146/annurev.earth.25.1.337.

Olsen, Paul E., Pamela J W Gore, and Roy W. Schlische. 1989. "Tectonic, Depositional, and Paleoecological History of Early Mesozoic Rift Basins, Eastern North America." In *28th International Geological Congress*, 174. Washington D.C.

Pálfy, József, Hungarian Natural, History Museum, and H- Budapest. 2000. "Synchrony between Early Jurassic Extinction , Oceanic Anoxic Event , and the Karoo-Ferrar Flood Basalt

Volcanism." *Geology* 28 (8): 747–50.

Poulton, Simon W., and Donald E. Canfield. 2005. "Development of a Sequential Extraction Procedure for Iron: Implications for Iron Partitioning in Continentally Derived Particulates." *Chemical Geology* 214 (3–4): 209–21. doi:10.1016/j.chemgeo.2004.09.003.

Power, M. R., D. Pirrie, and J. C. Ø. Andersen. 2003. "Diversity of Platinum-Group Element Mineralization Styles in the North Atlantic Igneous Province: New Evidence from Rum, UK." *Geological Magazine* 140 (5): 499–512. doi:10.1017/S0016756803008045.

Ripley, Edward M., and Chusi Li. 2003. "Sulfur Isotope Exchange and Metal Enrichment in the Formation of Magmatic Cu-Ni(PGE) Deposits." *Economic Geology* 98 (3): 635–41. doi:10.2113/gsecongeo.98.3.635.

Sackett, W M, S. Nakaparksin, and D. Dalrymple. 1970. "Carbon Isotope Effects in Methane Production by Thermal Cracking." In *Advances in Organic Geochemistry -1966*, edited by G. D. Hobson and G. C. Speers, 37–53. Pergamon Press.

Schlische, Roy W., and Paul E. Olsen. 1990. "Quantitative Filling Model for Continental Extensional Basins with Applications to Early Mesozoic Rifts of Eastern North America." *The Journal of Geology* 98 (2): 135–55. doi:10.1086/629390.

Schoell, Martin. 1984. "Recent Advances in Petroleum Isotope Geochemistry." *Organic Geochemistry* 6 (C): 645–63. doi:10.1016/0146-6380(84)90086-X.

Sepkoski, J John. 1996. "Patterns of Phanerozoic Extinction : A Perspective from Global Data Bases." *Global Events and Event Stratigraphy in the Phanerozoic*, 35–46. doi:10.1007/978-3-642-79634-0_4.

Smoot, J P. 1991. "Sedimentary Facies and Depositional Enviroments of Early Mesozoic Newark Supergroup Basins, Eastern North America." *Paleogeography, Palaeoclimatology, Palaeoecology* 84: 369–423.

Spear, Frank. 1993. *Metamorphic Phase Equilibria and Pressure-Temperature-Time Paths*. Washington, DC: Mineralogical Society of America.

Stookey, Lawrence L. 1970. "Ferrozine---a New Spectrophotometric Reagent for Iron." *Analytical Chemistry* 42 (7): 779–81. doi:10.1021/ac60289a016.

Stothers, Richard B. 1993. "Flood Basalts and Extinction Events." *Geophysical Research Letters* 20 (13): 1399–1402.

Svensen, Henrik H., Sverre Planke, Anders Malthe-Sorenssen, Bjørn Jamtveit, Reidun Myklebust, Torfinn Rasmussen Eidem, and Sebastian S. Rey. 2004. "Release of Methane from a Volcanic Basin as a Mechanism for Initial Eocene Global Warming." *Nature* 429 (June): 3–6. doi:10.1038/nature02575.1.

Tomkins, Andrew G. 2010. "Windows of Metamorphic Sulfur Liberation in the Crust: Implications for Gold Deposit Genesis." *Geochimica et Cosmochimica Acta* 74 (11). Elsevier Ltd: 3246–59. doi:10.1016/j.gca.2010.03.003.

Toulmin, Priestley, and Paul B Barton. 1964. "A Thermodynamic Study of Pyrite and

Pyrrhotite." *Geochimica et Cosmochimica Acta* 28 (5): 641–71. doi:10.1016/0016-7037(64)90083-3.

Viollier, E, P W Inglett, K Hunter, a N Roychoudhury, and P Van Cappellen. 2000. "The Ferrozine Method Revisited: Fe (II)/Fe (III) Determination in Natural Waters." *Applied Geochemistry* 15 (6): 785–90. doi:10.1016/S0883-2927(99)00097-9.

Wignall, Paul B. 2001. "Large Igneous Provinces and Mass Extinctions." *Earth-Science Reviews* 53: 1–33. doi:10.1130/2014.2505(02).

Wignall, Paul B. 2005. "The Link between Large Igneous Province Eruptions and Mass Extinctions." *Elements* 1 (5): 293–97. doi:10.2113/gselements.1.5.293.

Yallup, Christine, Marie Edmonds, and Alexandra V. Turchyn. 2013. "Sulfur Degassing due to Contact Metamorphism during Flood Basalt Eruptions." *Geochimica et Cosmochimica Acta* 120: 263–79. doi:10.1016/j.gca.2013.06.025.

Yamamoto, M. 1984. "Sulfur Isotope Effects in the Thermal Breakdown of Pyrite." *Earth Planetary Science Letters* 69, 335–34: 335–40.

Yoksoulian, Lois E. 2010. "Effect of Contact Metamorphism on Coal Geochemistry and Petrology: Implications for the Large Scale Release of 12C-Enriched Methane." University of Kentucky.

Zhabina, N.N., and I.I. Volkov. 1978. "A Method of Determination of Various Sulfur Compounds in Sea Sediments and Rocks." In *Environmental Biogeochemistry and Geomicrobiology Volume 3,* edited by Wolfgang Krumbein, 735–46. Ann Arbor: Ann Arbor Science.

Figure 1

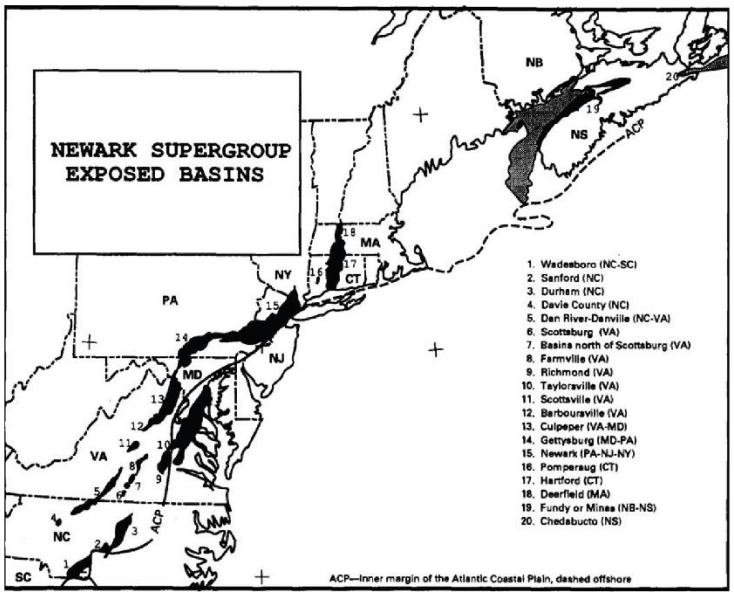

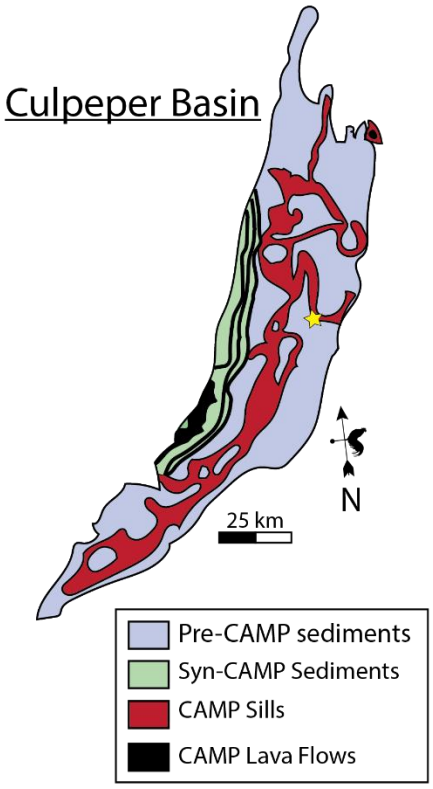

Figure 1: The figure on the left shows the exposed basins of the Newark Supergroup; the basin of interest (the Culpeper Basin) is labeled as number 13 (Smoot, 1991). The figure on the right is a simple schematic adaped from Marzoli et al., 2011 of the Culpeper Basin and the magmatic intrusions within it. The yellow star indicates our field site.

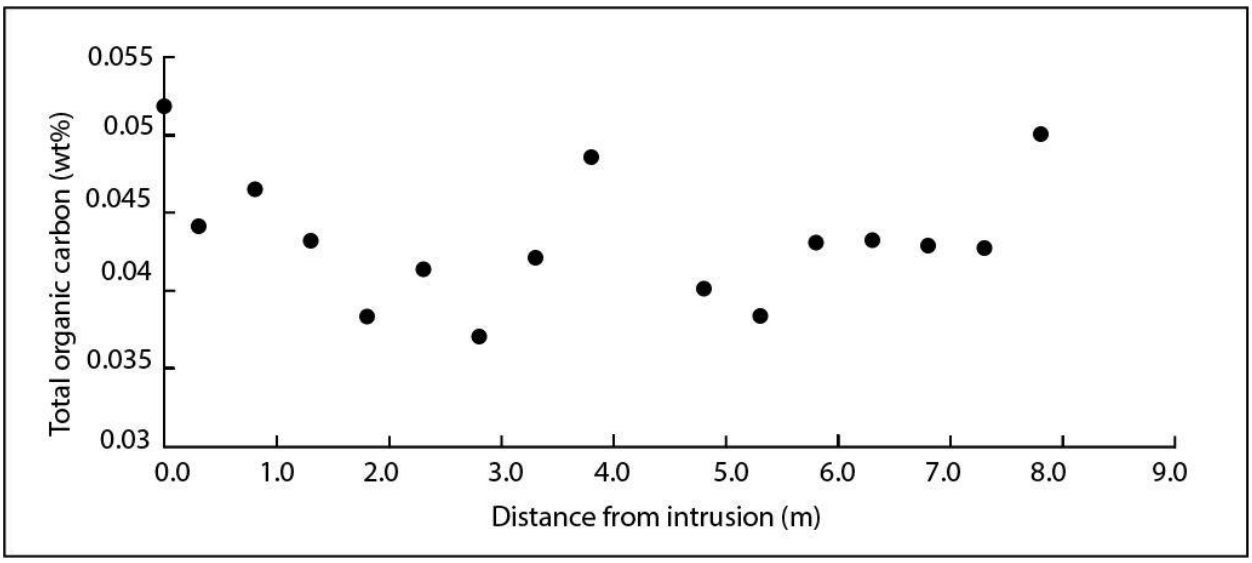

Figure 2: Total organic carbon content along Bed 1.

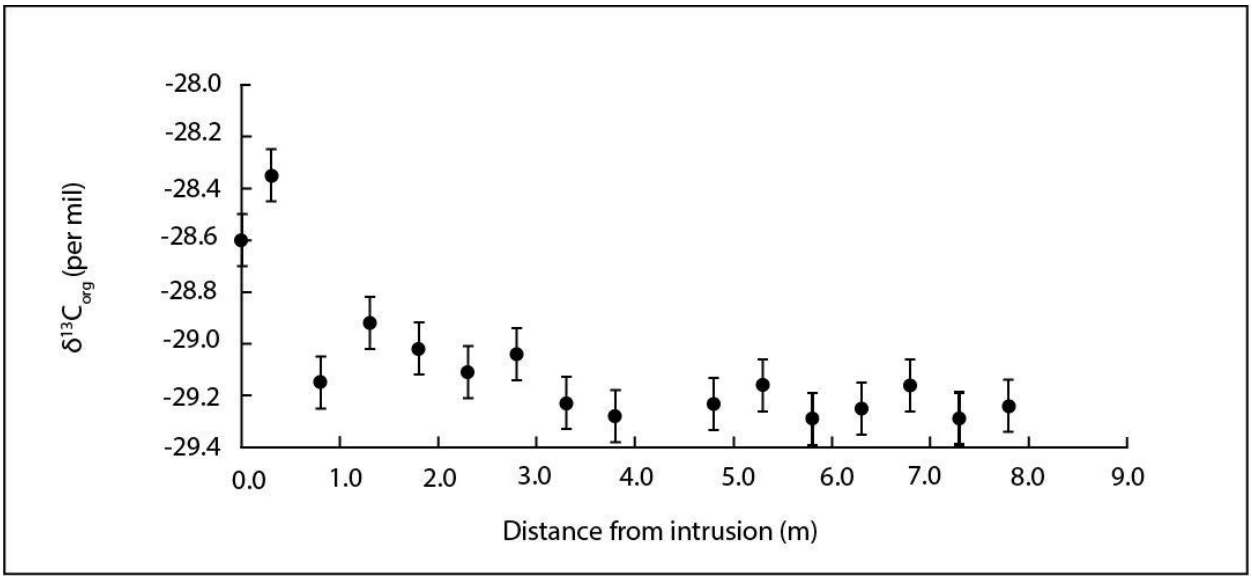

Figure 3: Organic carbon isotopic data from Bed 1 presented with the 1σ error bars.

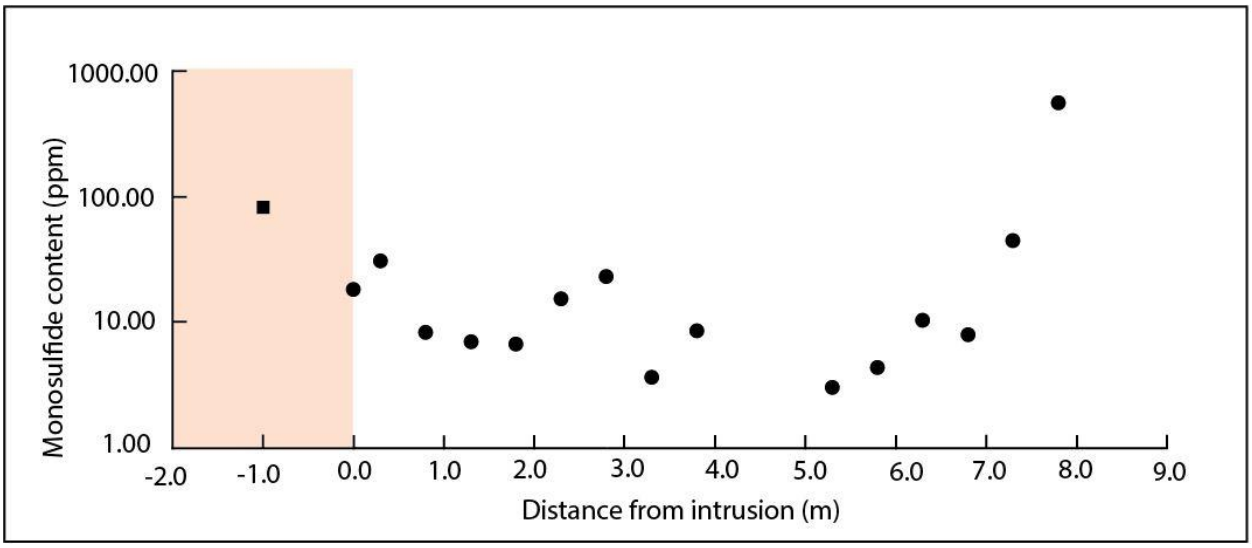

Figure 4: Monosulfide content in ppm with distance along Bed 1. The red box indicates the location of the dike and the square data point represents the monosulfide content of the dike and the circles represent the monosulfide content of the sedimentary transect. Error is smaller than the point.

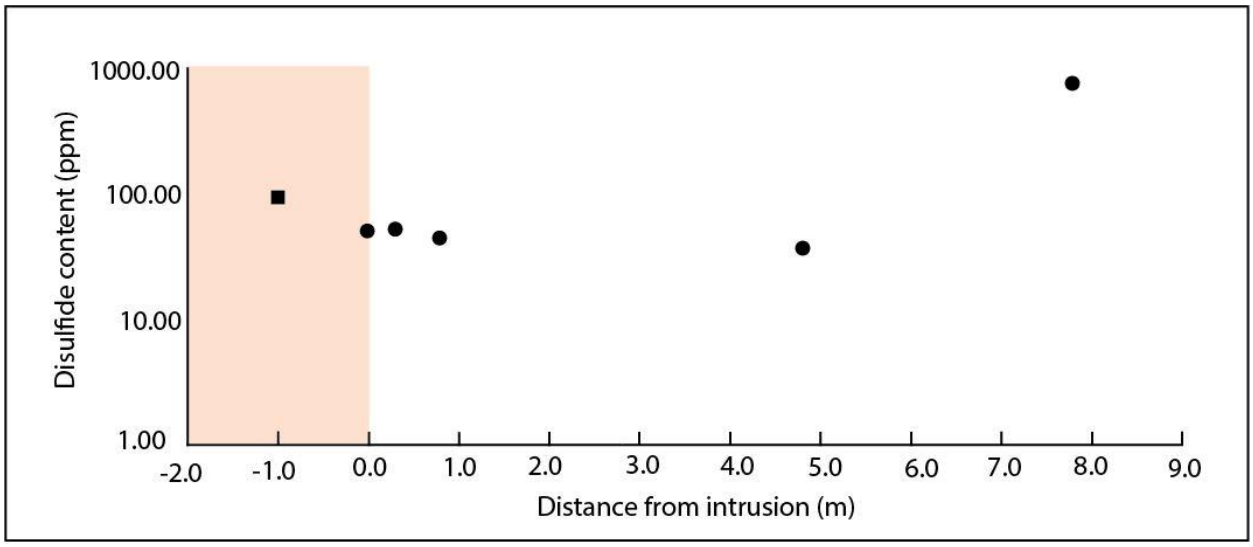

Figure 5: Disulfide content reported in ppm with distance along Bed 1. The red box indicates the location of the dike. The square data point represents the disulfide content of the dike and the circles represent the disulfide content of the sedimentary transect. Error is smaller than the point.

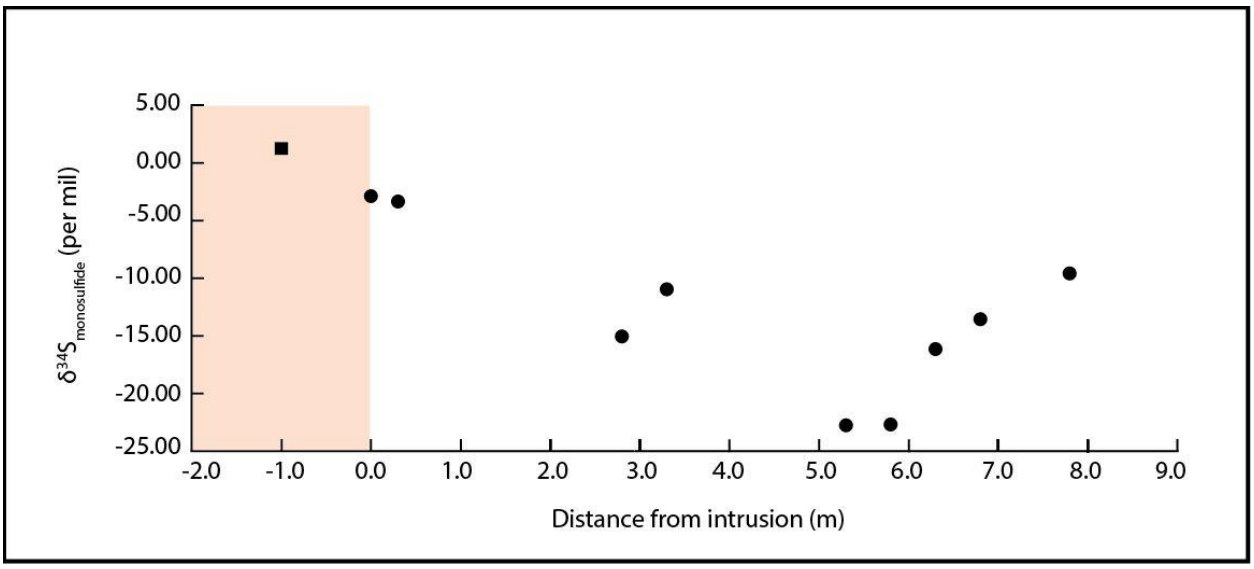

Figure 6: Sulfur isotopic composition of the extracted monosulfides reported in per mil. The red box indicates the dike and the square and circle data points are from the dike and sediments respectively. Error is smaller than the point.

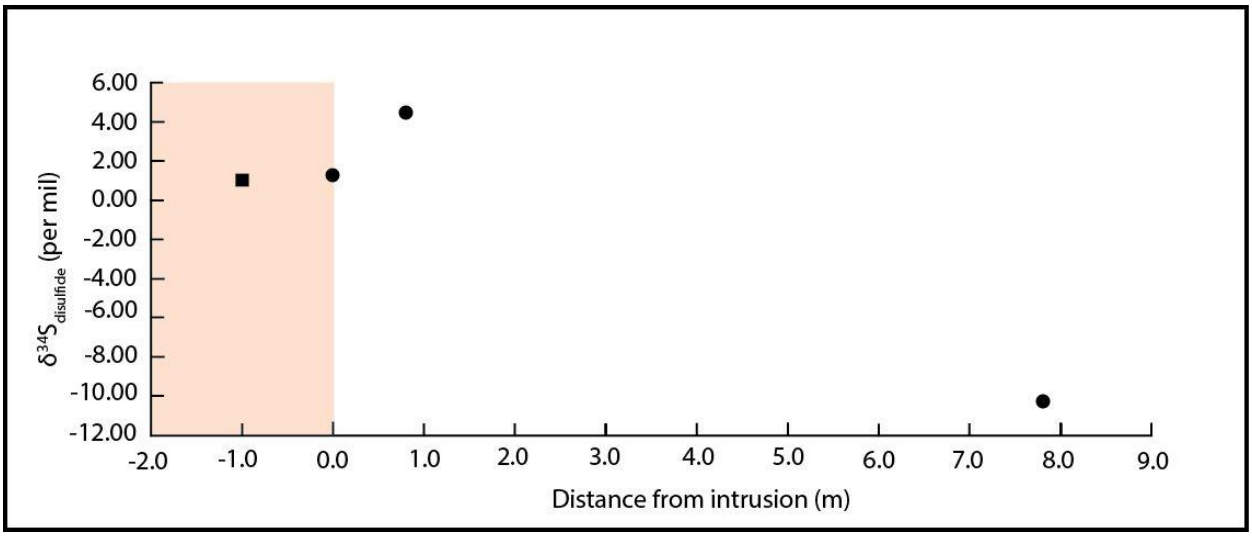

Figure 7: Sulfur isotopic composition of the extracted disulfides reported in per mil. The red box indicates the dike and the square and circle data points are from the dike and sediments respectively. Error is smaller than the point.

Sample ID	*Distance (m)*	*carb*	*ox*	*ur*
FQ-41	-1	0.3368	0.04141	2.78
FQ-1	0	0.1027	0.3796	3.19
FQ-2	0.3	0.0857	0.4440	3.76
FQ-3	0.8	0.0774	0.0594	2.09
FQ-4	1.3	0.1013	0.0875	2.06
FQ-5	1.8	0.0949	0.0481	2.55
FQ-6	2.3	0.0795	0.0547	2.29
FQ-7	2.8	0.0815	0.0957	2.68
FQ-8	3.3	0.0982	0.1059	2.30
FQ-9	3.8	0.0871	0.0879	2.33
FQ-10	4.8	0.0805	0.0645	2.16
FQ-11	5.3	0.0832	0.0541	2.06
FQ-12	5.8	0.1124	0.0508	2.07
FQ-13	6.3	0.1023	0.0577	2.07
FQ-14	6.8	0.0869	0.0234	2.41
FQ-15	7.3	0.1667	0.0506	2.18
FQ-16	7.8	0.2833	0.4787	3.48

Table 1: Iron carbonate (carb), iron oxide (ox) and unreactive iron (ur) data reported in weight percent. Distance column indicates distance from the intrusion. Sample FQ-41 is a sample of the dike itself.

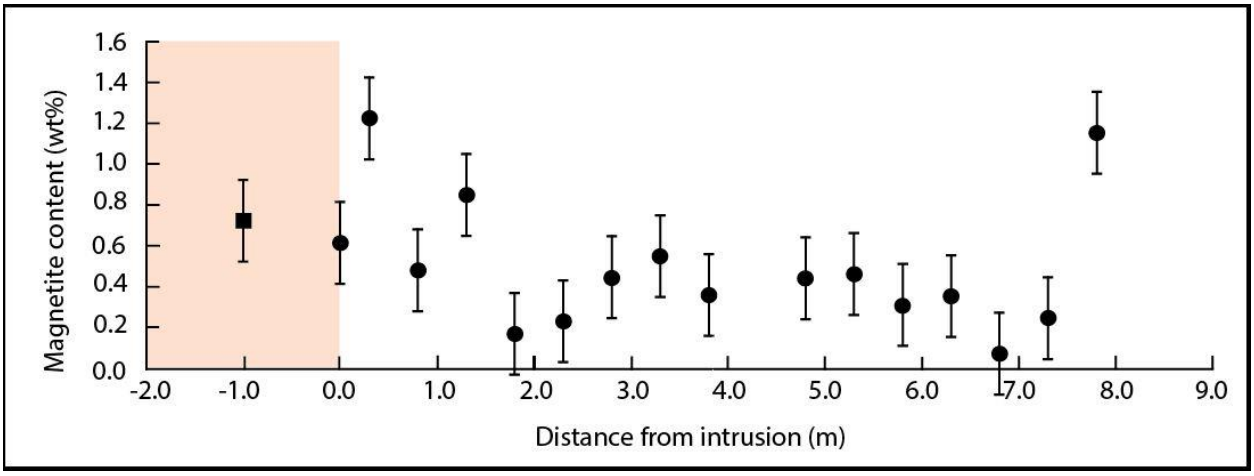

Figure 8: Magnetite content reported in weight percent. Error bars display 4% uncertainty as indicated in the methods section. The red box indicates the dike and the square and circle data points are from the dike and sediments respectively.

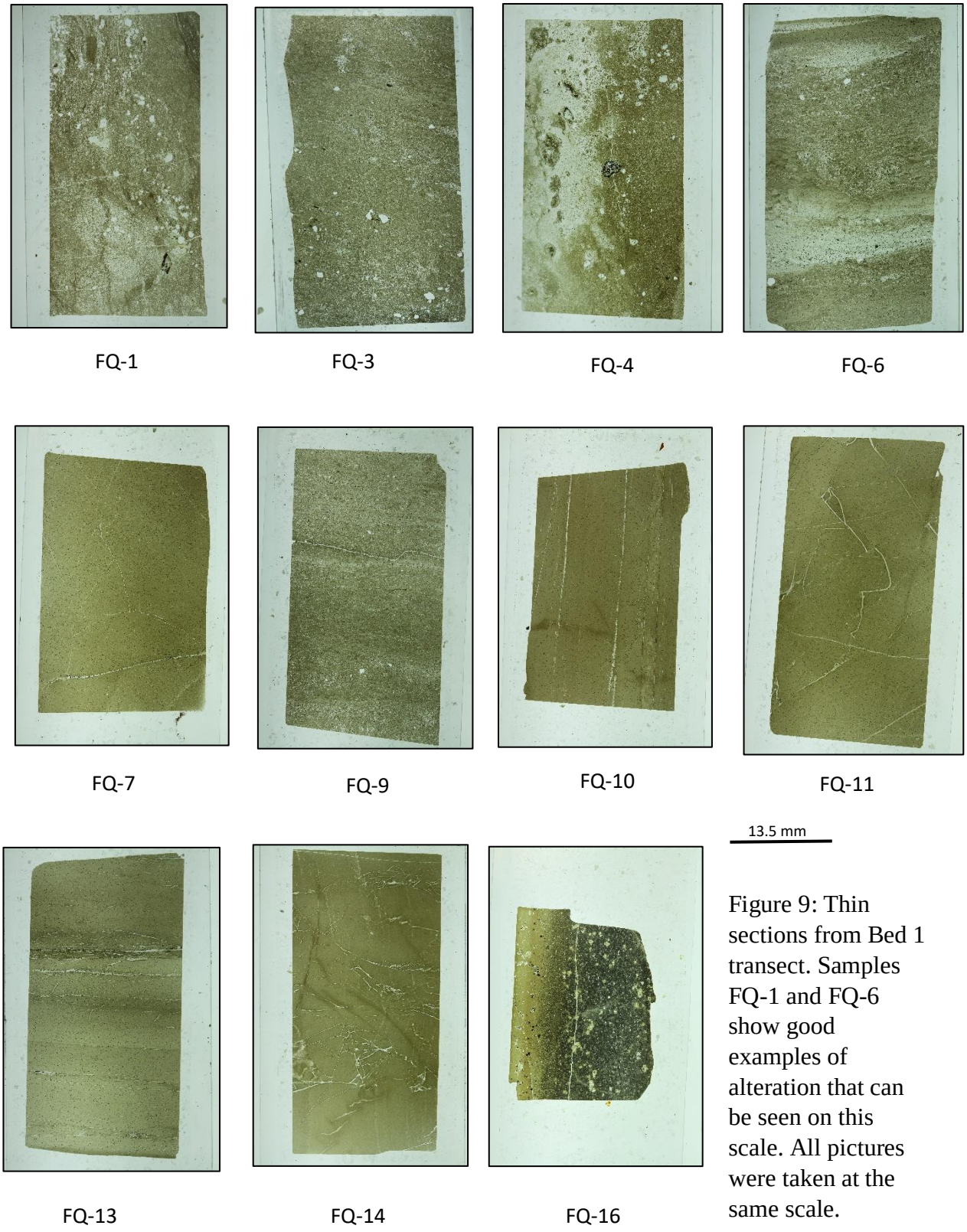

Figure 9: Thin sections from Bed 1 transect. Samples FQ-1 and FQ-6 show good examples of alteration that can be seen on this scale. All pictures were taken at the same scale.

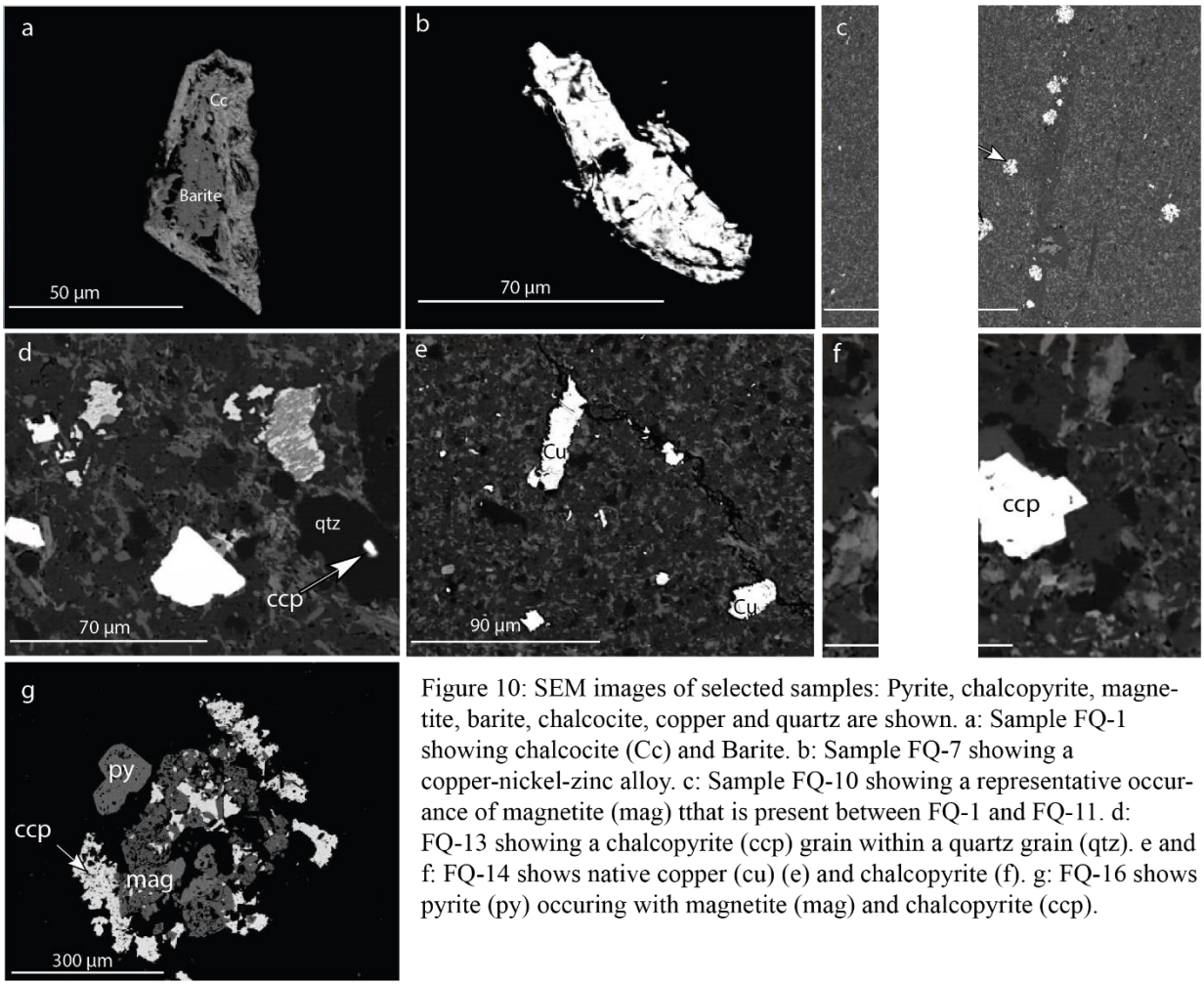

Figure 10: SEM images of selected samples: Pyrite, chalcopyrite, magnetite, barite, chalcocite, copper and quartz are shown. a: Sample FQ-1 showing chalcocite (Cc) and Barite. b: Sample FQ-7 showing a copper-nickel-zinc alloy. c: Sample FQ-10 showing a representative occurance of magnetite (mag) tthat is present between FQ-1 and FQ-11. d: FQ-13 showing a chalcopyrite (ccp) grain within a quartz grain (qtz). e and f: FQ-14 shows native copper (cu) (e) and chalcopyrite (f). g: FQ-16 shows pyrite (py) occuring with magnetite (mag) and chalcopyrite (ccp).

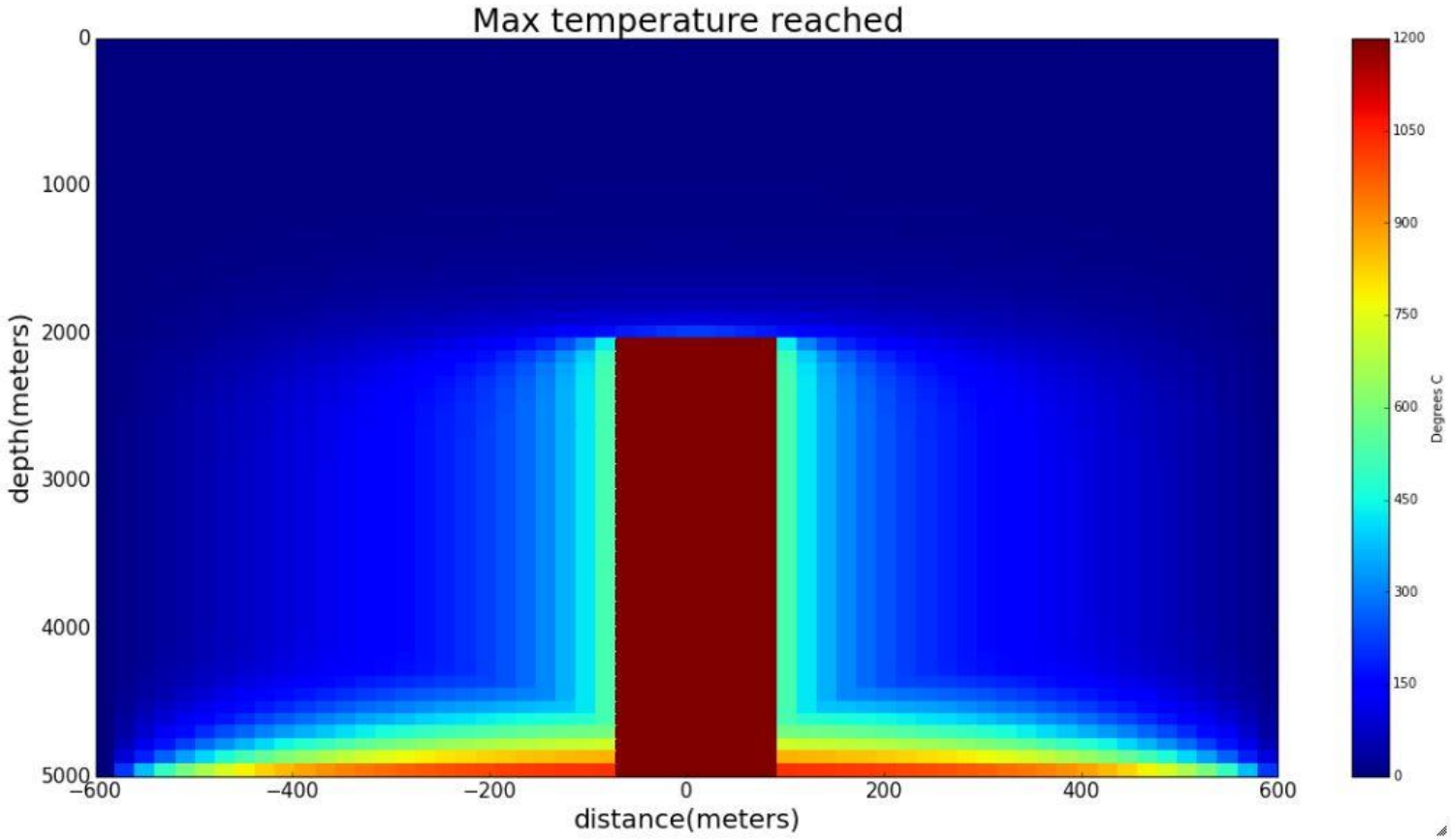

Figure 11: Two-dimensional thermal model of the dike emplaced at 1200˚C and its resulting contact aureole. x-axis shows distance from the center of the 170 m wide dike.

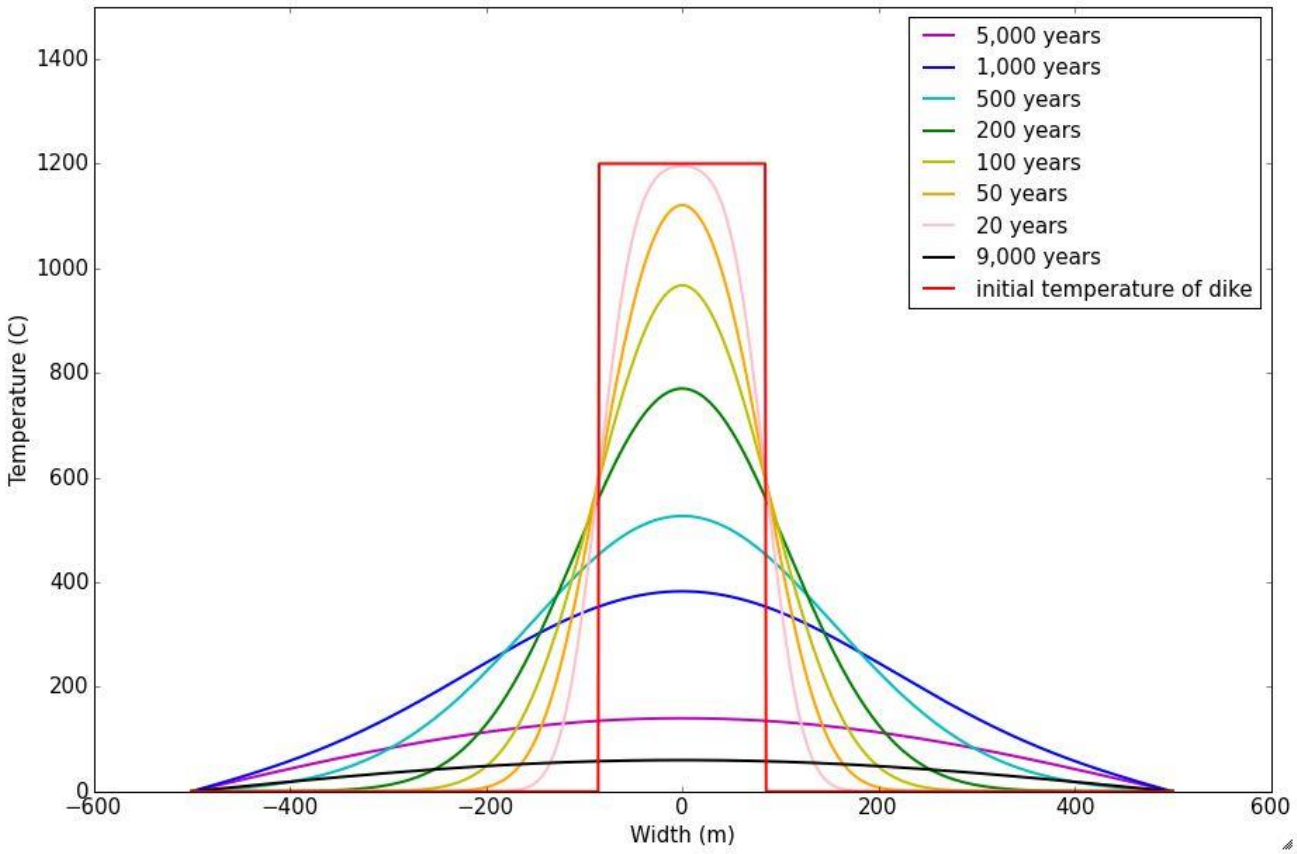

Figure 12a: one-dimensional model of the intrusion of the dike at 1200˚C. The contours show the cooling of the dike and the resultant temperature of the country rock after a certain amount of time specified in the legend.

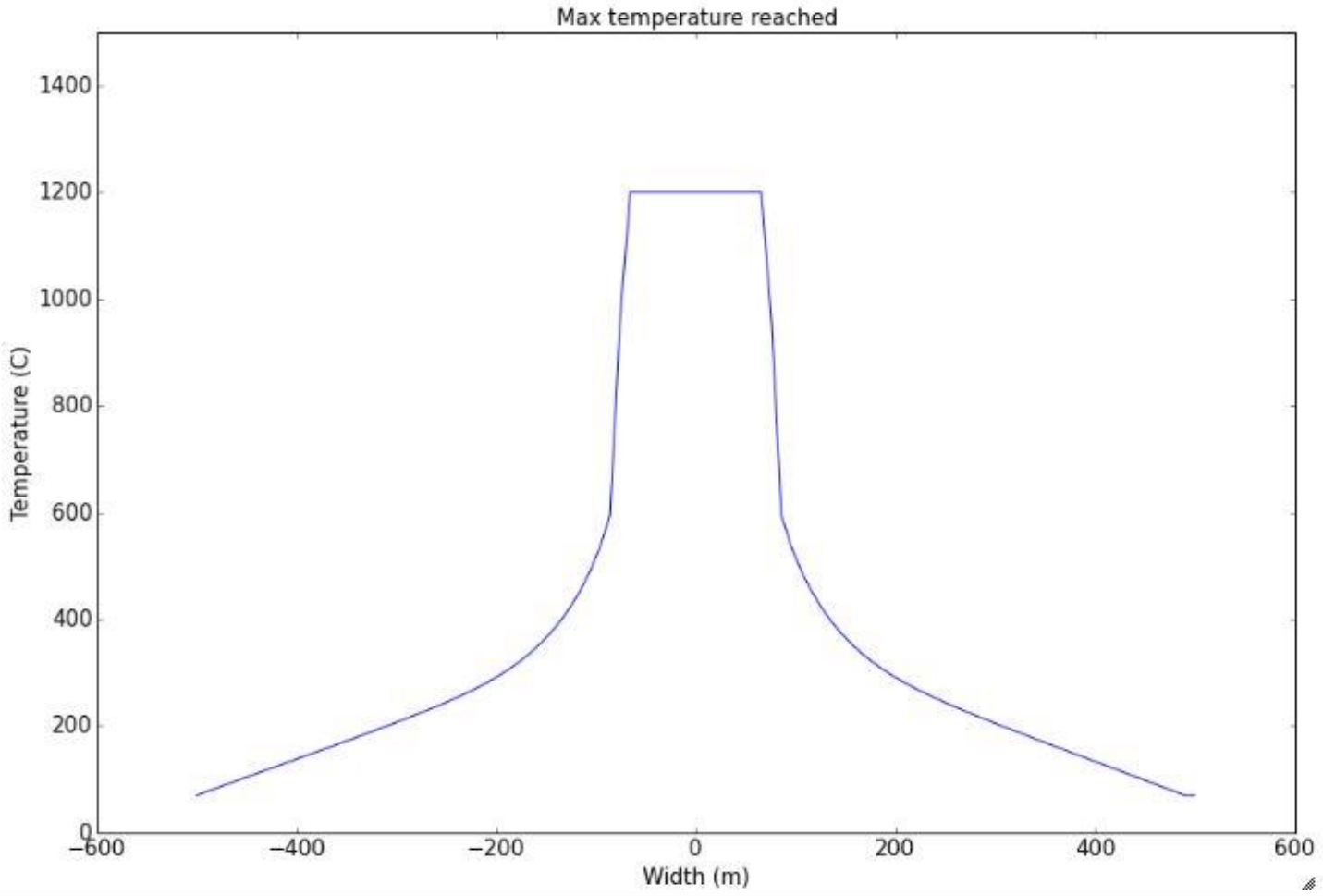

Figure 12b: one-dimensional thermal model showing the maximum temperature experienced by the country rock and dike in x-space.

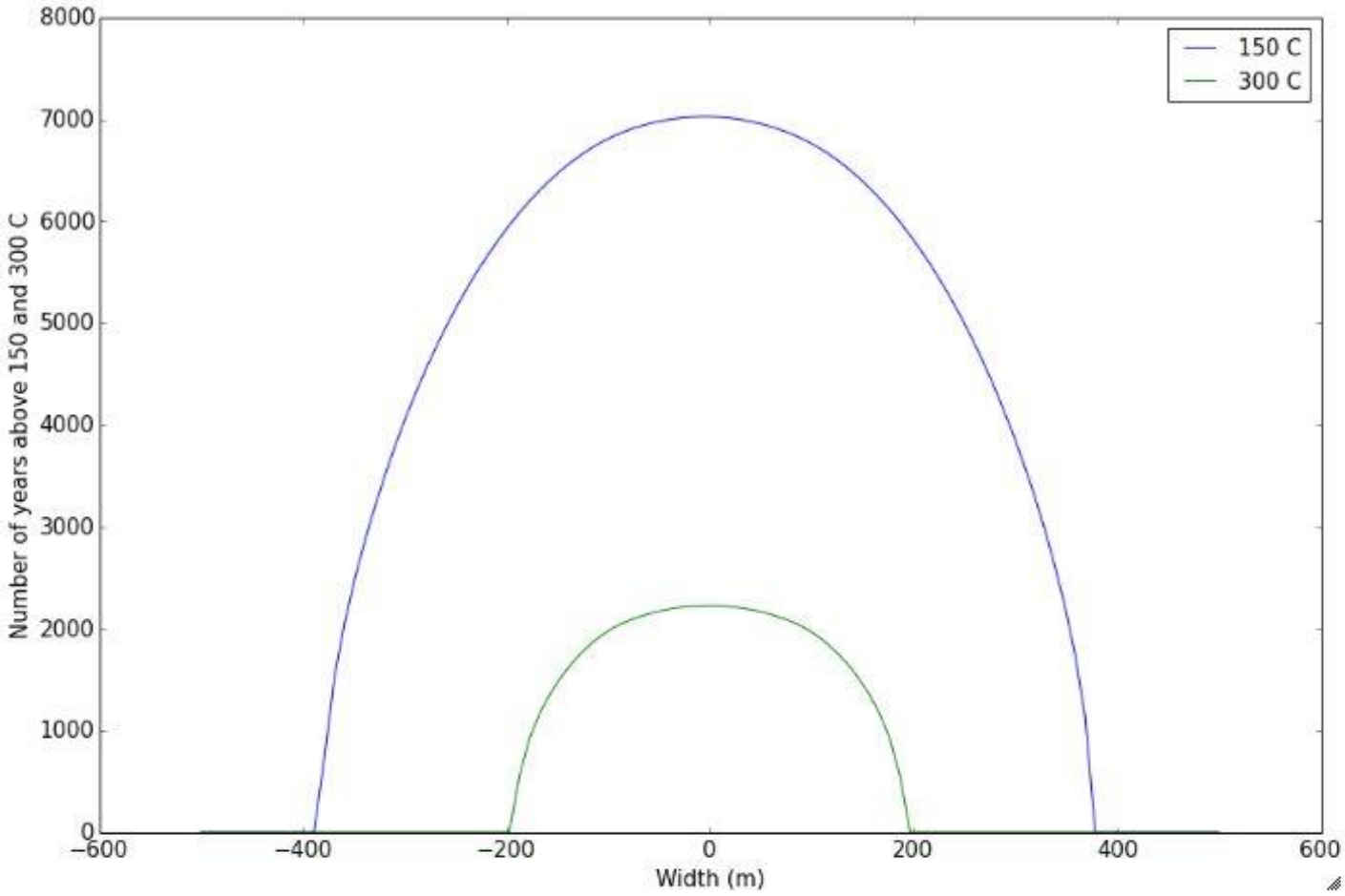

Figure 12c: one-dimensional thermal model showing the number of years that the country rock and dike experienced temperatures above 150˚C (blue) and 300˚C (green).

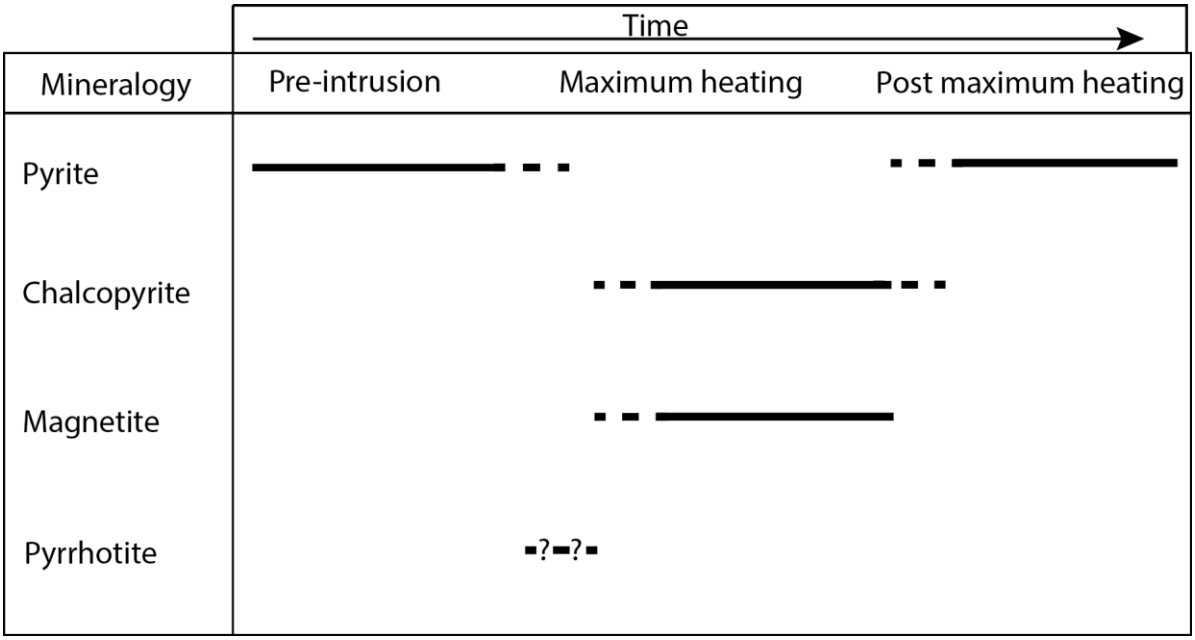

Figure 13: This paragenetic figure represents the different minerals that are present during different stages throughout time. This figure following the assumption that pyrite was present before the intrusion of the dike and then the intrusion allows for thermal breakdown of pyrite to pyrrhotite which is then converted to chalcopyrite and subsequently magnetite forms. Lastly after the heating has occurred there is a secondary phase of pyrite that forms.The dashed lines represent the break down and formation of minerals and the question marks indicate that we suspect this is when this mineral formed but we have no observation of it.

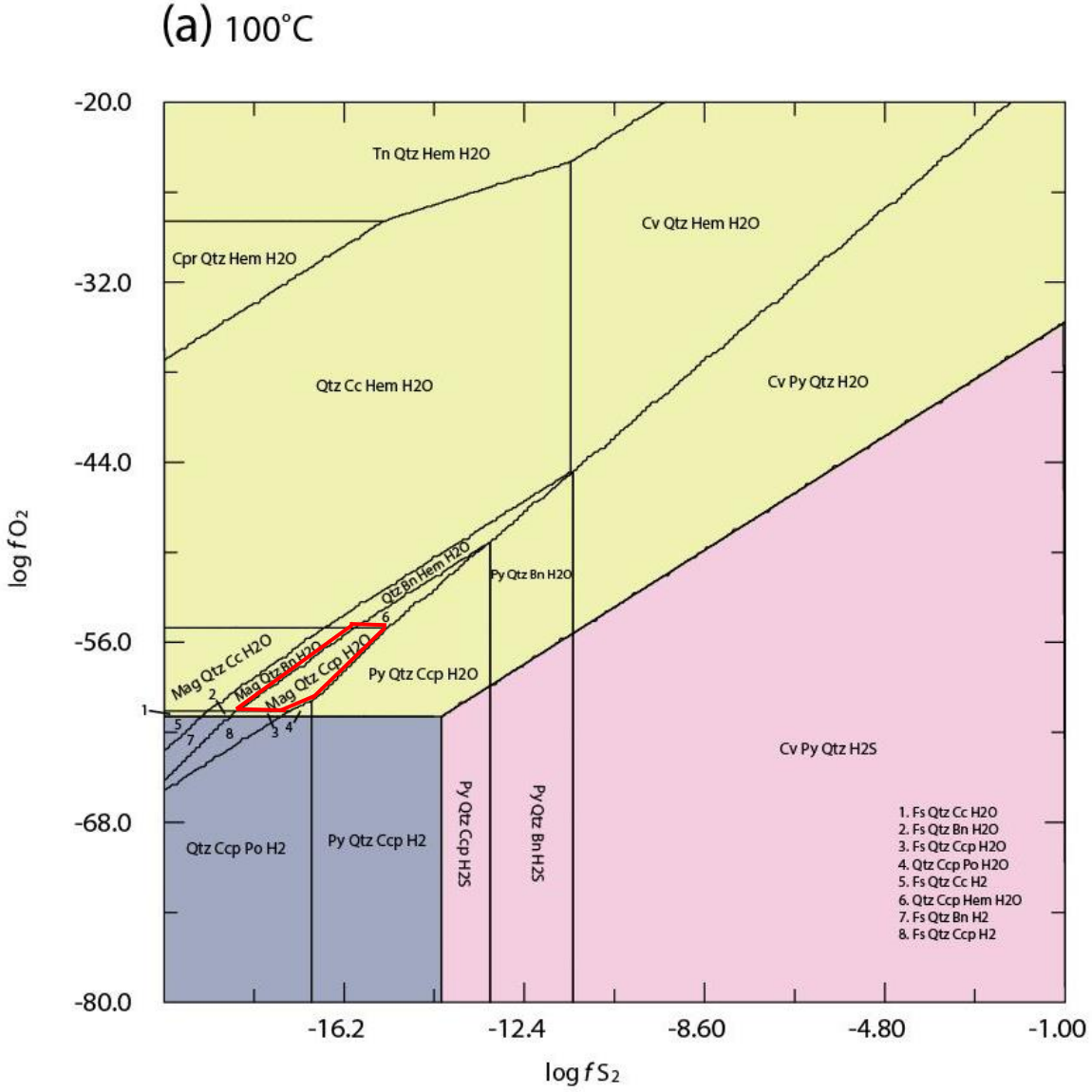

Figure 14 a: Model representing the stability fields at 100ºC for changing sulfur and oxygen fugacity using thermodynamic data set ctransf (Helgeson et al. 1978). Where the blue, yellow, and pink shaded areas represent the volatile species within that area (Blue = H_2 , Yellow = H_2O, and Pink = H_2S). Area surrounded in red indicates minerals that are seen in thin section. Abbreviations can be found in the Appendix.

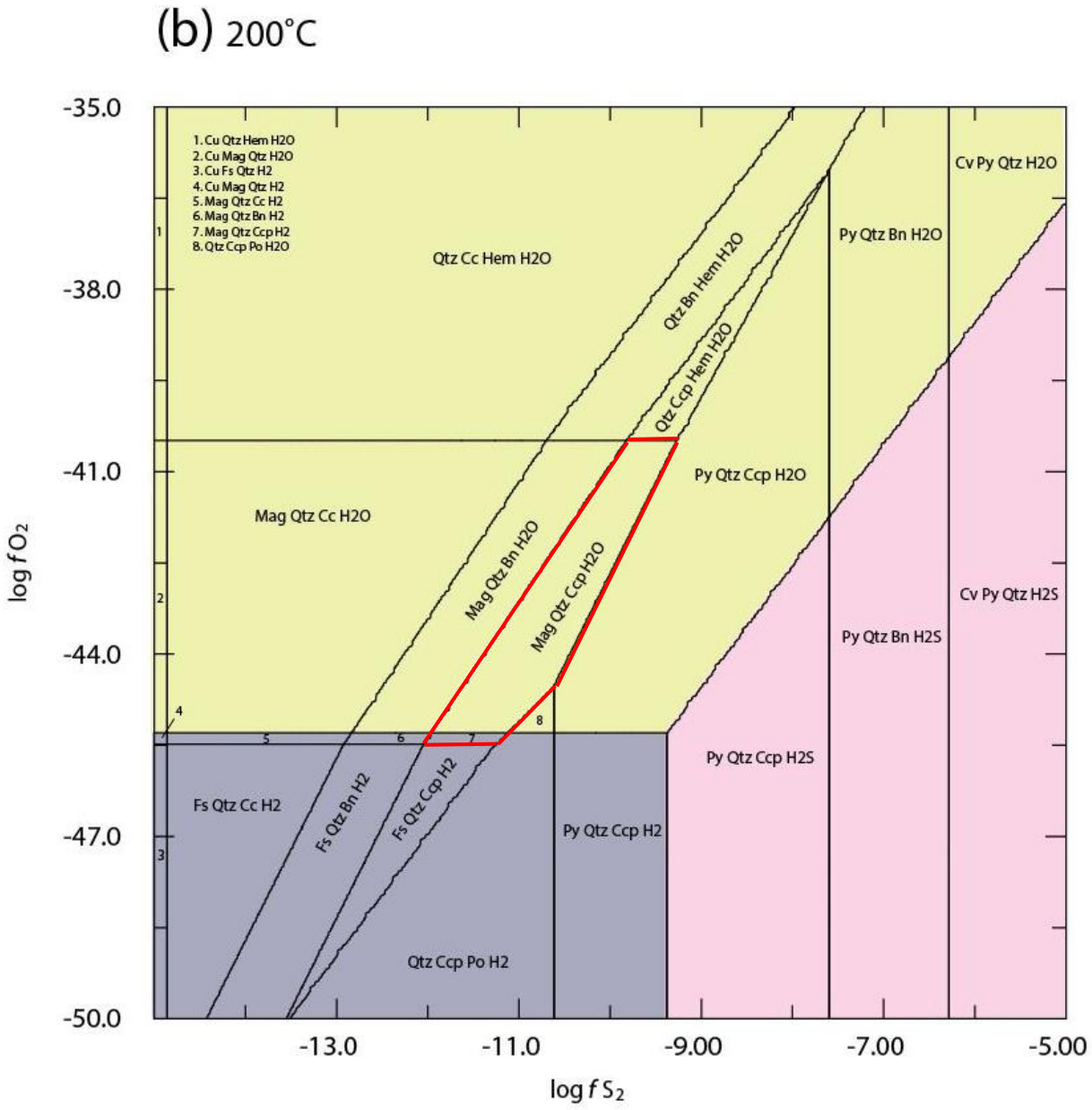

Figure 14 b: Model representing the stability fields at 200ºC for changing sulfur and oxygen fugacity using thermodynamic data set ctransf (Helgeson et al. 1978). Where the blue, yellow, and pink shaded areas represent the volatile species within that area (Blue = H_2 , Yellow = H_2O, and Pink = H_2S). Area surrounded in red indicates minerals that are seen in thin section.

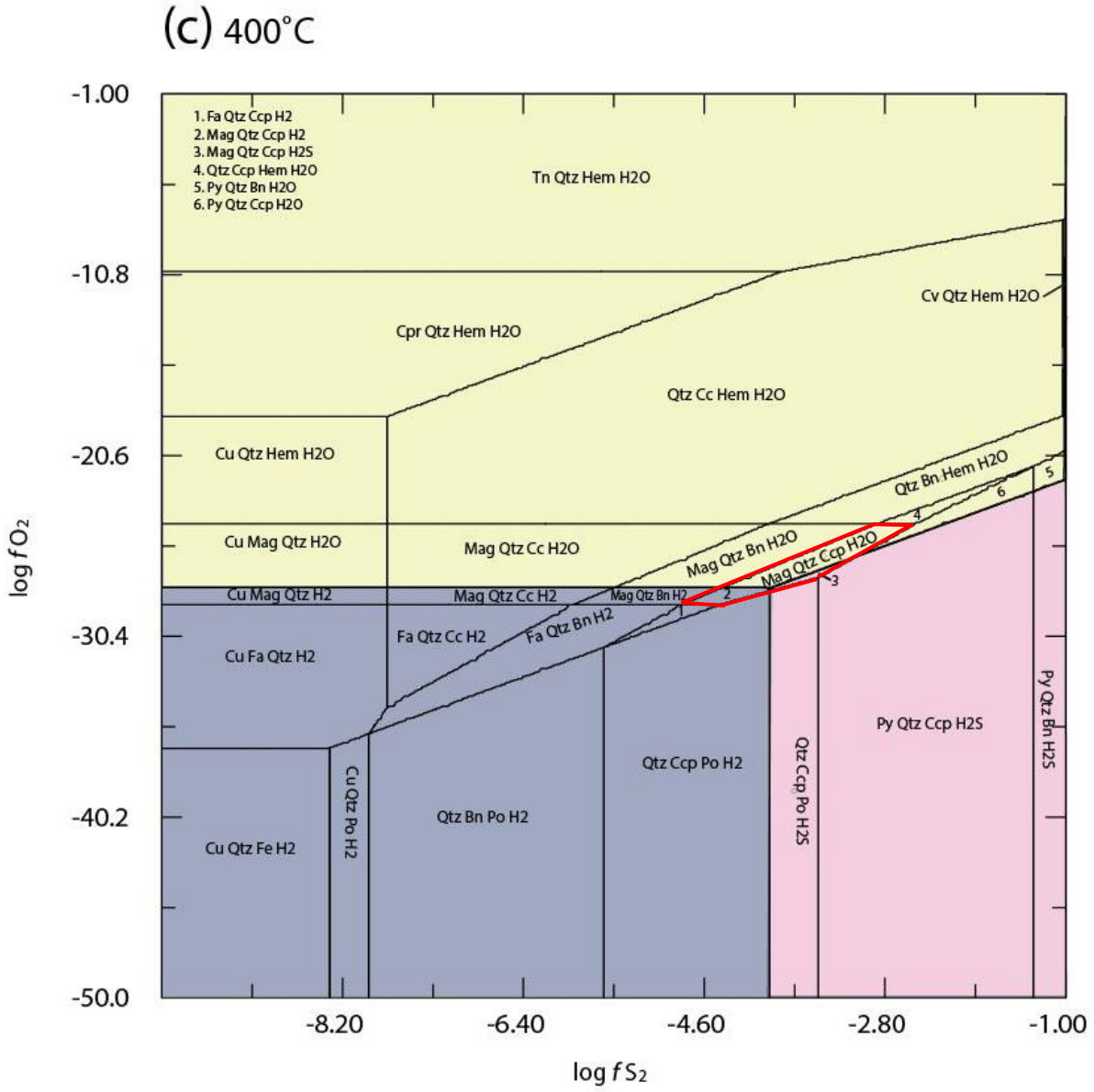

Figure 14 c: Model representing the stability fields at 400ºC for changing sulfur and oxygen fugacity using thermodynamic data set ctransf (Helgeson et al. 1978). Where the blue, yellow, and pink shaded areas represent the volatile species within that area (Blue = H_2 , Yellow = H_2O, and Pink = H_2S). Area surrounded in red indicates minerals that are seen in thin section.

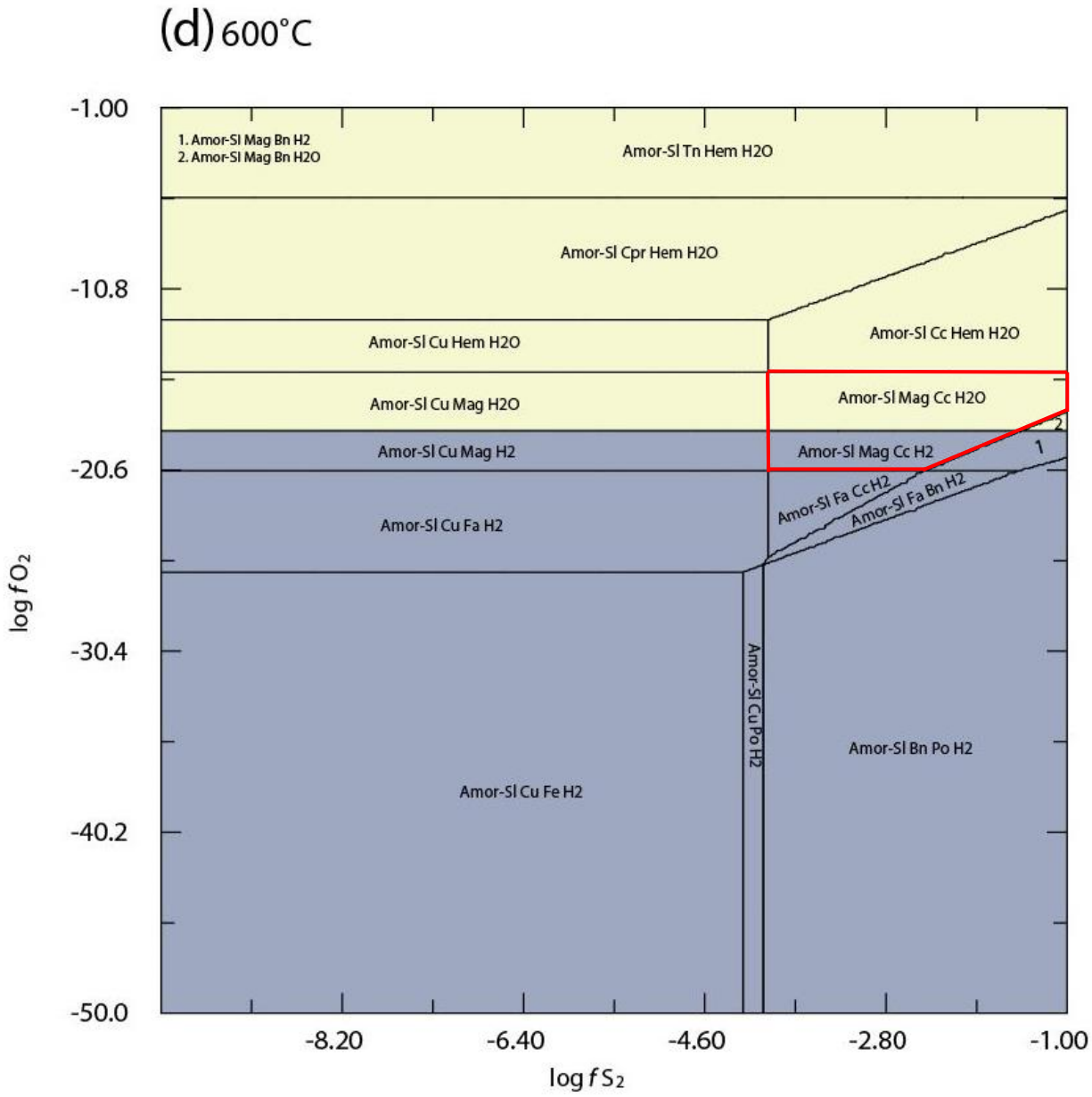

Figure 14 d: Model representing the stability fields at 600ºC for changing sulfur and oxygen fugacity using thermodynamic data set ctransf (Helgeson et al. 1978). Where the blue, yellow, and pink shaded areas represent the volatile species within that area (Blue = H_2 , Yellow = H_2O, and Pink = H_2S). Area surrounded in red indicates minerals that are seen in thin section.

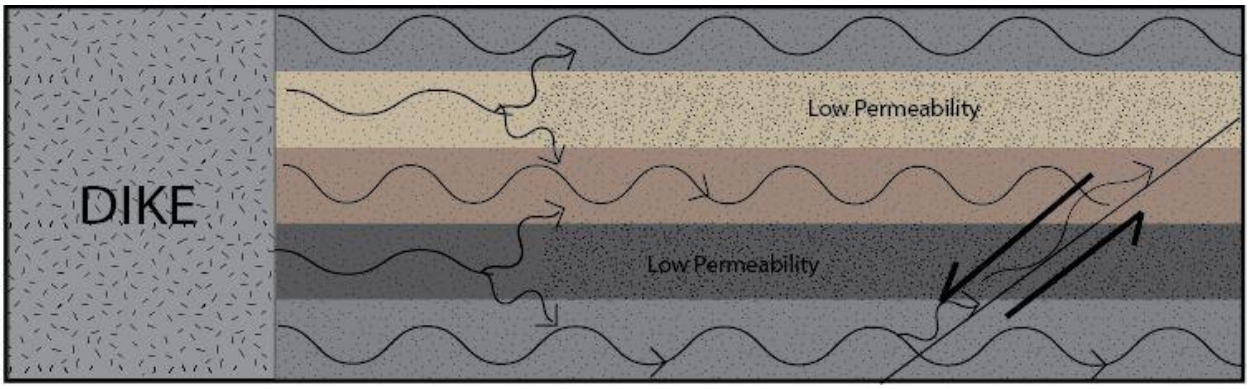

Figure 15: Illustrative model for the fluid flow within the sediments surrounding the dike. The dark gray bed represents the sampled bedding and the wavy lines with arrows representing fluid flowing through the sedimentary units. There are other potential mechanisms for enhancing fluid flow in the end of the dark gray bed such as fracturing.

Appendix A

Sample	*Distance from Intrusion (m)*	*Monosulfide S (ppm)*	*Disulfide S (ppm)*	*d34s mono*	*d34s disulfide*	*Iron carbonate*	*iron oxide*	*magnetite*	*unreactive iron*	*% org C*	$\delta^{13}C_{org}$
FQ-41	-1	83.40	95.53	1.23	1.04	0.34	0.04	0.72	2.78	-	-
FQ-1	0	18.45	51.32	-2.84	1.28	0.10	0.38	0.61	3.19	0.047	-28.83
FQ-2	0.3	31.13	53.03	-3.32	-	0.09	0.44	1.22	3.76	0.048	-28.68
FQ-3	0.8	8.38	45.63	-	4.50	0.08	0.06	0.48	2.09	0.050	-29.13
FQ-4	1.3	7.05	-	-	-	0.10	0.09	0.85	2.06	0.047	-29.09
FQ-5	1.8	6.75	-	-	-	0.09	0.05	0.17	2.55	0.051	-28.86
FQ-6	2.3	15.51	-	-	-	0.08	0.05	0.23	2.29	0.039	-29.22
FQ-7	2.8	23.34	-	- 15.02	-	0.08	0.10	0.44	2.68	0.039	-28.97
FQ-8	3.3	3.66	-	- 10.94	-	0.10	0.11	0.55	2.30	0.044	-29.28
FQ-9	3.8	8.62	-	-	-	0.09	0.09	0.36	2.33	0.050	-29.06
FQ-10	4.8	0.00	37.17	-	-	0.08	0.06	0.44	2.16	0.043	-29.08
FQ-11	5.3	3.04	-	- 22.76	-	0.08	0.05	0.46	2.06	0.049	-28.99
FQ-12	5.8	4.39	-	- 22.68	-	0.11	0.05	0.31	2.07	0.045	-29.10
FQ-13	6.3	10.52	-	- 16.12	-	0.10	0.06	0.35	2.07	0.048	-29.05
FQ-14	6.8	8.08	-	- 13.54	-	0.09	0.02	0.07	2.41	0.044	-29.08
FQ-15	7.3	45.29	-	-	-	0.17	0.05	0.25	2.18	0.055	-29.26
FQ-16	7.8	564.75	773.06	-9.57	-10.23	0.28	0.48	1.15	3.48	0.053	-29.25
FQ-17	7.8	65.30	97.76	-3.50	-5.12	0.11	0.05	0.46	2.85	0.031	-27.70
FQ-18	8.3	112.33	922.36	-4.07	-4.69	0.18	0.05	0.21	2.92	0.039	-27.28
FQ-19	8.8	413.15	3514.40	-4.64	-4.51	0.22	0.04	0.15	3.46	0.098	
FQ-20	9.3	49.76	3.21	-3.98	-5.32	0.16	0.03	0.14	3.32	0.024	
FQ-21	9.8	214.62	2610.71	-5.30	-4.90	0.17	0.04	0.21	3.62	0.066	
FQ-22	10.3	37.44	25.81	- 10.16	-12.07	0.15	0.05	0.36	3.30	0.028	
FQ-23	11.3	6.52	-	-4.82	-	0.08	0.09	1.10	3.03	0.021	
FQ-24	12	20.54	-	-5.34	-	0.08	0.09	1.09	2.70	0.022	
FQ-25	12.5	20.25	4.56	-6.34	-1.37	0.08	0.10	1.04	2.60	0.024	
FQ-26	13	0.00	-	-4.54	-	0.09	0.08	0.79	2.60	0.020	
FQ-27	14.1	19.81	-	-2.66	-	0.22	0.28	1.20	2.75	0.028	
FQ-28	14.6	21.25	4.43	2.75	4.89	0.11	0.06	0.60	3.28	0.030	
FQ-29	15.9	46.11	6.51	2.40	-0.88	0.15	0.10	0.84	3.62	0.025	
FQ-30	15.9	46.55	-	-	-	0.21	0.02	0.12	4.39	0.030	
FQ-31	17.2	21.88	-	4.13	-	0.26	0.04	0.52	3.71	0.052	
FQ-32	17.6	18.16	-	3.75	-	0.20	0.02	0.17	3.61	0.021	
FQ-33	18.1	29.63	-	-0.64	-3.34	0.21	0.05	0.87	3.54	0.033	
FQ-34	18.6	29.06	-	6.47	-	0.28	0.03	0.17	4.31	0.019	
FQ-35	19.3	0.00	3.88	7.74	6.27	0.32	0.04	0.31	3.62	0.029	

FQ-36	19.9	0.00	-	4.37	-	0.21	0.02	0.16	4.11	0.016
FQ-37	20.4	0.00	-	7.11	-	0.24	0.03	0.17	4.31	0.022
FQ-38	20.9	0.00	-	5.83	-	0.28	0.04	0.34	3.86	0.020
FQ-39	21.4	29.27	23.81	1.54	1.14	0.21	0.05	0.80	4.03	0.026
FQ-40	21.9	10.66	-	6.74	-	0.22	0.03	0.19	4.13	0.028
FQ-42	200	0.00	-	-	-	0.19	0.04	0.30	2.88	0.024
FQ-43	250	8.90	-	-	-	0.15	0.04	0.27	3.02	0.024
FQ-44	300	0.00	-	-	-	0.05	0.29	0.29	2.99	0.023

Appendix B

Abbreviations for phase diagrams:

Abbreviation	Name	Mineral Formula
Amor-SI	Amorphous silica	SiO_2
Bn	Bornite	Cu_5FeS_4
Cc	Chalcocite	Cu_2S
Ccp	Chalcopyrite	$CuFeS_2$
Cpr	Cuprite	Cu_2O
Cu	Copper	Cu^0
Cv	Covellite	CuS
Fa	Fayalite	Fe_2SiO_4
Fs	Ferrosilite	$Fe_2Si_2O_6$
H_2	Hydrogen	H_2
H_2O	Water	H_2O
H_2S	Hydrogen sulfide	H_2S
Hem	Hematite	Fe_2O_3
Mag	Magnetite	Fe_3O_4
Po	Pyrrhotite	Fe_7S_8
Py	Pyrite	FeS_2
Qtz	Quartz	SiO_2
Tn	Tenorite	CuO

Python Code for 1D:

```
from scipy import *
import numpy as np
import matplotlib.pyplot as plt
year=(60*60*24*356.25)
Magma_Temperature = 1200.
Country_Rock_Temperature = 70.
Density = 2640. #kg/m^3 density of country rock
Thermal_Conductivity = 1.6 # W/mK Eppelbaum et al 2014, Clark 1966 and Blackwell et al 1989
Specific_Heat_Capacity = 870.#of the country rock Eppelbaum et al 2014
K = (Thermal_Conductivity/(Density*Specific_Heat_Capacity))
nx=100
x = np.linspace(-500, 500,nx) # controls x-axis
```

```
dx=abs(x[1]-x[0])
print dx
ntime=10000 #number of time steps
time=np.linspace(0,10000*year,ntime)
dtime=(time[1]-time[0])
r=((K*dtime)/(dx**2))
print r
Temperature=np.ones([ntime,nx])*Country_Rock_Temperature
for i in range(nx):
   if x[i] >= -85 and x[i] <= 85:
      Temperature[0,i]=Magma_Temperature
for j in range(1,ntime):
   for i in range(1, nx-2):
      Temperature[j,i]=(Temperature[j-1, i]+K*dtime/dx**2.0*(Temperature[j-1, i-1]-2.*Temperature[j-1,
i]+Temperature[j-1, i+1]))
plt.figure(figsize = (15,10) )
plt.plot(x,Temperature[-1,:],'k', label = "9,000 years", linewidth=2) #last timestep
plt.plot(x,Temperature[5000,:],'m', label = "5,000 years", linewidth=2)# 5000  years
plt.plot(x,Temperature[1000,:],'b', label="1,000 years", linewidth=2)# 1000 years
plt.plot(x,Temperature[500,:],'c', label = "500 years", linewidth=2) #500 years
plt.plot(x,Temperature[200,:],'g', label = "200 years", linewidth=2) #250 years
plt.plot(x,Temperature[100,:],'y', label = "100 years" , linewidth=2) #125 years
plt.plot(x,Temperature[50,:], color= 'orange', label = "50 years", linewidth=2) #62.5 years
plt.plot(x,Temperature[20,:], color= 'pink', label = "20 years", linewidth=2) #62.5 years
plt.plot(x,Temperature[0,:],'r', label = "initial temperature of dike", linewidth=2) #first time step
plt.ylim([0,1500])
plt.xticks(fontsize=15)
plt.yticks(fontsize=15)
plt.legend(fontsize= 15)
plt.ylabel("Temperature (C)", fontsize = 15)
plt.xlabel("Width (m)", fontsize = 15)
plt.show()
MaxTemp = np.ones([nx])*Country_Rock_Temperature
for j in range(1,ntime):
   for i in range(1,nx-2):
      if Temperature[j,i] > MaxTemp[i]: #documents the max temp
            MaxTemp[i] = Temperature[j,i]
plt.figure(figsize = (15,10))
plt.plot(x,MaxTemp[:])
plt.ylim([0,1500])
plt.xticks(fontsize=15)
plt.yticks(fontsize=15)
plt.legend(fontsize= 15)
plt.ylabel("Temperature (C)", fontsize = 15)
plt.xlabel("Width (m)", fontsize = 15)
plt.title("Max temperature reached", fontsize = 15)
plt.show()
Temp300 = zeros([nx])
```

```
Temp150 = zeros([nx])
for i in range(0,nx):
   d = 0
   c=0
   for j in range (1, ntime):
      if Temperature[j,i]> 300:
         d=d+1
      if Temperature[j,i]> 150:
         c=c+1
   Temp150[i]= c
   Temp300[i]= d
plt.figure(figsize = (15,10))
plt.plot(x,Temp150[:], label = "150 C")
plt.plot(x,Temp300[:], label = "300 C")
plt.xticks(fontsize=15)
plt.yticks(fontsize=15)
plt.legend(fontsize= 15)
plt.ylabel("Number of years above 150 and 300 C", fontsize = 15)
plt.xlabel("Width (m)", fontsize = 15)
plt.show()
```

Python code for 2D:

```
import scipy
from scipy import *
from numpy import*
from pylab import rcParams
import matplotlib.pyplot as plt
"""All units are in kilograms, meters, seconds, Celsius/Kelvin"""
year=(60*60*24*365) #establish a year in seconds
Magma_Temperature = 1200. # initial magma temperature
Density = 2640. #kg/m^3 density of country rock
Thermal_Conductivity = 1.6 # W/mK
Specific_Heat_Capacity = 870.#of the country rock Eppelbaum et al 2014
K = (Thermal_Conductivity/(Density*Specific_Heat_Capacity))
print K
"""Grid Spacing(in meters)"""
nx = 60 #how many sections you are dividing x into
ny = 60 #how many sections you are dividing y into
y = np.linspace (0,5000,ny) #estalishing the y axis range (depth of 5km)
dy = abs(y[1]-y[0])
dy2=dy**2
x = np.linspace(-600,600,nx) #estalishing the x axis range (length of .2km)
dx = abs(x[1]-x[0])
dx2=dx**2
print dx #grid spacing in x direction meters
print dy
#stabilizes time
```

```
dtime=dx2*dy2/(2*K*(dx2+dy2))/8.9028
print dtime
time = arange(0,10000.*year,dtime) #time interval of 10000 years
ntime=len(time)
print len(time), time[-1]/(60*60*24*365.)
"""Define Steady State Crustal Geothermal Gradient"""
Temperature=zeros([ntime, nx, ny])
Temperature_Surface = 20.

for n in range (ntime):
      for j in range(ny):
         Temperature[n,j] = Temperature_Surface+ (25*(0.001*y))
plt.plot(Temperature[n,j],y)
plt.xlabel("Temperature(Celsius)")
plt.ylabel("depth(meters)")
plt.gca().invert_yaxis()
plt.show
##Pressure in Pa (kg per meter per second per second),convert to kbar
#time is implemented here so that you can include erosion.
Pressure = zeros([ntime,ny])
Gravity = 9.8
Pressure_Surface = 0.001

for n in range (ntime):
   for j in range (ny):
      Pressure[n,j] = ((Pressure_Surface + Density * Gravity * y[j])*(1.E-8))

plt.plot(Pressure[n,:],y)
plt.xlabel("Pressure (kbar)")
plt.ylabel("depth(meters)")
plt.gca().invert_yaxis()
plt.show
print Pressure.shape
"""Boundaries of Intrusion"""
for i in range(nx):
   for j in range(ny):
      if x[i] >= -85 and x[i] <= 85 and y[j] >= 2000 and y[j] <= 5000: # all of these bounds are in
meters so we have a 170m wide and 1000km deep dike
         Temperature[0,i,j]=Magma_Temperature
"""Loop to run numerical approximation of 2D diffusion equation"""
for n in range(1,ntime):
   for i in range(1, nx-1):
      for j in range (1, ny-1):
         term1 = (Temperature[n-1, i+1, j] - 2.*Temperature[n-1, i, j] + Temperature[n-1, i-1,
j])/dx2
```

```
        term2 = (Temperature[n-1, i, j+1] - 2.*Temperature[n-1, i, j] + Temperature[n-1, i, j-
1])/dy2
        Temperature[n, i, j]= Temperature[n-1, i, j] + (dtime*K*(term1 + term2))
#Boundary Conditions for magma
   for i in range(nx):
      Temperature[n,i,-1]=Magma_Temperature #defines the magma reservoir beneath intrusion
MaxTemp = zeros([nx,ny])
for n in range(0,ntime):
   for i in range(0,nx):
      for j in range (1, ny):
         if Temperature[n,i,j] > MaxTemp[i,j]: #documents the max temp
            MaxTemp[i,j] = Temperature[n,i,j]
print Temperature[100,1,2]
plt.subplot(321)
plt.figure(figsize=(20,10))
plt.pcolormesh(x,y,transpose(MaxTemp))
plt.colorbar(orientation= 'vertical',label = "Degrees C")
plt.ylabel("depth(meters)", fontsize = 20)
plt.xlabel("distance(meters)", fontsize = 20)
plt.title("Max temperature reached", fontsize = 25)
plt.yticks(fontsize=15)
plt.xticks(fontsize = 15)
plt.gca().invert_yaxis()
```